Evaluation of the non-Newtonian lattice Boltzmann model coupled with off-grid bounce-back scheme: Wall shear stress distributions in Ostwald–de Waele fluids flow

Hamed Vaseghnia,[1,*] Espen Jettestuen,[2] Knut Erik Teigen Giljarhus,[3] Olav Aursjø,[4] and Aksel Hiorth[1]
[1]*Department of Energy Resources, University of Stavanger, Stavanger N-4036, Norway*
[2]*NORCE Norwegian Research Centre, Oslo N-0166, Norway*
[3]*Department of Mechanical and Structural Engineering and Materials Science, University of Stavanger, Stavanger N-4036, Norway*
[4]*NORCE Norwegian Research Centre, Stavanger N-4068, Norway*

(Received 22 February 2024; accepted 13 June 2024; published 15 July 2024)

We present a comprehensive analysis of the non-Newtonian lattice Boltzmann method (LBM) when it is used to simulate the distribution of wall shear stress (WSS). We systematically identify sources of numerical errors associated with non-Newtonian rheological behavior of fluids in off-grid geometries. We implement the single relaxation time, Bhatnagar-Gross-Krook (BGK), and multiple relaxation time (MRT) collision operators and investigate flow in a two-dimensional channel aligned with lattice directions and off-grid Hagen-Poiseuille flow of Ostwald–de Waele (power-law) fluids. As for boundary conditions, we implement constant body force-driven and pressure-driven flows. These two boundary conditions have different numerical challenges, which include numerical stability, accuracy, mass conservation, and compressibility effects, which are inherent in the LBM method. Our results indicate that MRT, when the relaxation times are adequately tuned in the non-Newtonian case, significantly improves the WSS distribution accuracy and the numerical stability of the LBM. MRT also enhances the stability and accuracy for non-Newtonian fluids compared with the Newtonian case, meaning that it is questionable if a BGK collision operator is appropriate to use in a non-Newtonian case with off-grid boundaries. When analyzing the non-Newtonian LBM in the context of staircase walls and interpolated bounce-back (IBB) walls, a MRT collision operator with the appropriate choice of tunable relaxation times makes it possible to achieve numerically accurate results without a significant increase in grid resolution for matching to the analytical solution of WSS distributions.

In analyzing the non-Newtonian flows, we show that the viscosity dependency of bounce-back walls in the BGK-LBM deviates from the results obtained under Newtonian assumptions. The power-law index further influences these discrepancies, and errors caused by the viscosity dependency of the bounce-back boundary conditions can be effectively mitigated by implementing the MRT procedure. Results show that non-Newtonian fluids, in contrast with the Newtonian assumption, encounter a greater mass imbalance when flowing through a periodic system with IBB walls. MRT can address this challenge, as it allows for independent adjustments of physical relaxation times and enhances mass conservation in the case of non-Newtonian fluids. In pressure-driven non-Newtonian flows, there is a significant impact of bulk viscosity. This aspect is often overlooked in Newtonian simulations but can significantly impact fluid adapting to rapid changes in local effective viscosity. One of our main conclusions is that the MRT collision operator with tuned relaxation times can effectively resolve numerical problems caused by non-Newtonian rheological properties and off-grid geometries. We also provide practical guidelines for selecting the most suitable simulation approach.

DOI: 10.1103/PhysRevE.110.015305

I. INTRODUCTION

Wall shear stress (WSS) must be precisely modeled for simulation tools to work well, especially when dealing with non-Newtonian fluids in industrial and medical applications. In a biomedical context and non-Newtonian blood rheology, it has been discovered that WSS plays a pivotal role in remodeling the endothelium, the inner layer of vascular walls [1]. The remodeling process of the endothelium can assist in understanding the underlying cause of vascular diseases and atherosclerosis [2]. The relationship between the mechanical impact on vascular walls and the onset of vascular disease can be quite complex. Consequently, it is imperative for simulation tools to model WSS accurately. In the case of Newtonian fluids, WSS can be easily determined by examining the linear relationship between the velocity gradient of the fluid at the boundary and the stress. However, when dealing with non-Newtonian fluids, the relationship between stress and strain becomes nonlinear, leading to complexities [3]. Non-Newtonian fluids exhibit various characteristics, including shear-dependent viscosity, viscoelasticity, and the ability to undergo thixotropy or rheopexy [4]. Generalized Newtonian fluid models can accurately describe the predominant behavior observed in most non-Newtonian fluids, which exhibit shear-thinning or thickening characteristics. In this

*Contact author: hamed.vaseghnia@uis.no

framework, the viscosity of the fluid is not constant but varies with the shear strain rate, as dictated by the constitutive equations of the stress tensor.

In recent years, several numerical techniques have been proposed to model the intricate behavior of non-Newtonian fluid flows [5–7]. Among them, the lattice Boltzmann method (LBM) has emerged as a viable alternative to conventional Navier-Stokes solvers. This is primarily due to its advantageous features, including low computational cost, capabilities of parallel programming, and ability to handle wall boundary conditions locally [8,9]. The LBM also has a unique characteristic that enables calculating the local components of the stress tensor in fluid flow without estimating velocity gradients, which is necessary for Navier-Stokes solvers [10]. This property of LBM is helpful in various simulation applications, including non-Newtonian fluid dynamics and multiscale and multiphase flows. Calculating the shear rate locally makes simulations more accurate and detailed, particularly in places with complicated shapes and high velocity gradients. By facilitating a more thorough and accurate understanding of fluid behavior across a range of scales and flow conditions, this approach increases the practicality of LBM in addressing various fluid dynamics problems such as WSS modeling. These attributes have contributed to the increasing use of the LBM in analyzing non-Newtonian fluids [11–16].

The implementation of the hydrodynamic boundary conditions at the level of the mesoscopic distribution functions of LBM and fluid-solid interactions has been the subject of numerous theoretical and numerical studies [17–20]. The deployment of boundary conditions, numerical accuracy, and kinetic-theory analysis of specific models were some of the topics covered in these investigations. The simple bounce-back technique, suggested by Ladd [21], provides the foundation for most later refined bounce-back designs and has been extensively used for fluid-solid interaction problems in LBM simulations. The primary idea of the bounce-back rule is that, when a lattice particle at a boundary node moves toward a solid surface along a link, it reverses direction upon contacting the boundary. As a result, the unknown distribution function is the incident distribution function plus a term that accounts for the impact of wall velocity [22]. The bounce-back scheme technically differs from other approaches that require stability treatment and ensures solution stability even when approaching the instability limit of relaxation times [23]. Also, mass conservation at stationary boundaries is rigorously ensured since bounce-back relies on reflections, which is crucial, especially in problems where total mass plays a significant role [24]. However, it has been shown that the bounce-back condition only ensures greater-than-first-order precision if the wall passes halfway through the lattice links and the surface is aligned with the lattice discrete directions [22]. Both criteria are violated in curved and nonplanar boundary configurations where the wall cuts the lattice connections at different distances and the bounce-back becomes first-order accurate. A simple approach for handling complex no-slip boundaries using the bounce-back scheme is to approximate them with a staircase shape. This approach requires a higher resolution in the computational domain to prevent unfavorable inaccuracies caused by stair-shaped approximations and artificial wall roughness [25]. Bouzidi *et al.* [18] presented an enhanced scheme to achieve higher accuracy by modifying the bounce-back enclosure rule by implementing interpolation schemes. These schemes require nonlocal surface smoothing processes, which allow the generation of off-grid boundary locations from voxel data and enable the resolution of the actual boundary location with subgrid precision [25]. The proposed scheme effectively maintains second-order accuracy in the solution and proves to be computationally efficient for resting boundaries. However, this approach has some limitations. Since the reflection of particle distributions relies on boundary locations and interpolations rather than directly reflecting the particles, there is a risk of violating mass conservative characteristic of the bounce-back approach.

Furthermore, combining the bounce-back method and the Bhatnagar-Gross-Krook (BGK) collision model introduces a dependence on viscosity for accurately determining the placement of the no-slip boundary [26]. Consequently, using the bounce-back scheme in this scenario may introduce additional error terms that are not accounted for in the standard Chapman-Enskog analysis [27]. One implication of these errors is the emergence of a small slip velocity at the solid wall in continuum flows, which is associated with relaxation rates [22,28]. This effect becomes even more pronounced in complex fluids modeled using the LBM, where relaxation rates are nonconstant, and the fluid does not strictly adhere to Newton's law of viscosity. Therefore, addressing numerical issues in the features of the LBM becomes crucial, especially when dealing with non-Newtonian fluids and WSS distributions on off-grid wall boundaries.

The behavior of the WSS in LBM simulations was carefully examined for the first time by Stahl *et al.* [25]. They proposed a scheme to calculate the normal wall vectors necessary for determining WSS. In that study, the primary cause of the inaccuracy was revealed to be the distortion of the velocity field near the staircase boundaries. In inclined two-dimensional (2D) Poiseuille and Womersley flows, Kang and Dun [29] investigated the accuracy of the WSS for BGK and multiple relaxation time (MRT) collision operators coupled with halfway and interpolated bounce-back (IBB) methods. They reported similar results for BGK and MRT with the selected parameters. Shimogonya *et al.* [30] proposed a hemodynamic index for predicting the onset of a cerebral aneurysm using LBM. They define this index as the temporal fluctuations of tension forces exerted on endothelial cells. Using the bounce-back boundary method and LBM, Kang [31] examined the error of WSS measurements in oscillatory blood flows. Kang [31] indicated that blood flow simulations should be performed at a very high resolution since WSS measurements should be carried out at a specific distance from the wall. However, to the best of our knowledge, WSS distributions of the non-Newtonian fluids and the complexity of the fluids behavior have been overlooked in the existing literature. It has been shown empirically that using a Newtonian viscosity model may underestimate WSS, as the shear-thinning effects of the fluids lead to an increase in WSS, and accordingly, more careful treatments should be done in these measurements and studies [32,33]. Note that the accuracy of WSS measurements highly depends on the choice of alternative wall boundary conditions. Curved boundary assessments and WSS evaluations may be possible with other approaches,

including immersed boundary [34] and ghost cell methods [35,36]. While, in this paper, we focus mainly on the popular bounce-back technique, additional investigation is necessary to develop improved boundary conditions that enable accurate WSS calculations using other aproaches.

In this paper, we comprehensively evaluate the conventional BGK and MRT collision operators within the context of the D2Q9 non-Newtonian LBM to simulate WSS distributions. Our evaluation is based on the application to the off-grid Hagen-Poiseuille flow of Ostwald–de Waele fluids, also known as power-law fluids. The selection of Ostwald–de Waele fluids for this paper is motivated by the availability of analytical solutions, enabling a detailed and comprehensive analysis of the performance of the numerical solver in simulating these complex fluid behaviors. A spectrum of generalized Newtonian models exists, including the Carreau, Carreau-Yasuda, Herschel-Bulkley, Cross, and Casson models, which can accurately model shear-viscosity profiles tailored to specific problems [37–39]. However, the absence of analytical solutions for these models prevents their direct inclusion in this paper. Nevertheless, the analyses conducted in this paper are expandable to all non-Newtonian models coupled with LBM, and the application of these models can affect the accuracy of results.

The evaluation focuses on two distinctive flow scenarios of constant body force- and pressure-driven flows. We aim to identify and comprehend the sources of errors associated with each scenario and the behavior of complex fluids through a systematic analysis. Specifically, we investigate various aspects such as numerical stability, accuracy, mass conservation, and mitigating compressibility effects inherent in the LBM.

The remaining sections of this paper are organized as follows: In Sec. II, we present challenges in the non-Newtonian LBM and the assessment procedure. In the first part of Sec. III, we thoroughly assess the sources of numerical errors and instabilities in the non-Newtonian LBM in aligned channel flows. We scrutinize its capabilities and limitations to understand its applicability comprehensively. Subsequently, in the second part of Sec. III, we examine a detailed analysis of the sources of numerical errors and instabilities that arise in the context of non-Newtonian fluid flows and the off-grid bounce-back method. We also explore potential techniques to mitigate these issues using MRT as an advanced collision operator. Finally, in Sec. IV, we summarize the essential findings and provide conclusive remarks based on the research conducted throughout this study.

II. METHODOLOGY

A. Tracing errors in LBM coupled with non-Newtonian fluid model

Due to the bounce-back condition at walls, an imbalance in the distribution of particles is created and generates a momentum transfer, which gives rise to WSS. The LBM uses the bounce-back scheme for walls aligned with its Cartesian grid, but this method inaccurately represents curved boundaries as stair shaped walls, increasing computational costs due to the need for finer grids. The IBB [18] method addresses this by interpolating functions from nearby nodes to accurately model curved boundaries, enhancing accuracy and efficiency in LBM simulations. Fluid dynamics and flow conditions near solid boundaries influence these interpolated values. However, due to the interpolation process, there is a loss of information regarding the precise fluid state at the boundaries, which leads to a mass imbalance issue. This nonconservative behavior can lead to spurious flows or inaccuracies in simulations, especially in periodic systems driven by forces, without additional treatments for mass conservation. For non-Newtonian fluids, the accuracy of the boundary condition is even more critical because the viscosity is not constant and can vary significantly throughout the domain. Therefore, it is essential to address mass conservation of the non-Newtonian fluids in periodic systems.

In the context of LBM, the BGK collision approach has been successfully used in various fluid mechanics applications. It exhibits instabilities at high Reynolds numbers and introduces a dependency on viscosity at the wall boundaries when coupled with the bounce-back scheme. Instabilities arise from the evolution of moments of the distribution function that cannot be directly linked to physical quantities in fluid mechanics [23,40]. d'Humières [23] proposed the MRT approach to address this flaw by substituting a matrix for the scalar relaxation time. The main idea behind MRT collision is to independently relax each moment and transform the collision step into momentum space. This approach helps to prevent instabilities caused by the temporal expansion of these unphysical moments [41].

Additionally, bulk viscosity measures the resistance of a fluid to volume changes under compression or expansion. Its adjustment is available as an independent tunable parameter offered by the MRT collision operator. In these cases, the bulk viscosity represents energy dissipation due to volume changes. Also, it is known that LBM recovers the Navier-Stokes equations with an assumption of small compressibility originating from the underlying kinetic theory [42], which can be affected by the bulk viscosity relaxation modifications. Since viscosity variations in non-Newtonian fluids lead to different wave and pressure propagation patterns, accurately adjusting the bulk viscosity relaxation time is vital for precise fluid flow simulations.

Accordingly, in this paper, we address the challenges mentioned with non-Newtonian fluids by conducting a systematic study using the Hagen-Poiseuille flow. The methodology involves investigating BGK and evaluating various physical moments offered by the MRT collision operator and their interactions with the complex rheological behavior of non-Newtonian fluids in different flow conditions.

B. The lattice Boltzmann structure

In the hydrodynamic regime, the lattice Boltzmann technique provides a solution for the Boltzmann transport equation. It can be obtained using a finite-order spectral technique to discretize the Boltzmann equation. Consequently, the features of the resulting system of connected hyperbolic equations are integrated. The result is the formulation of the widely recognized lattice Boltzmann equation:

$$f_i(\vec{x} + e_i\delta t, t + \delta t) - f_i(\vec{x}, t) = \Omega_i, \tag{1}$$

where f_i defines the density distribution function with discrete velocity e_i along the ith direction in the population space of the particles. Here, t represents the time, x represents the spatial coordinate, and Δt is the time step. Also, Ω is the collision operator, signifies viscous and nonlinear effects, and defines how molecule collisions lead to the rebalancing of the distribution function. For this paper, we restrict ourselves to 2D LBM with nine discrete velocity directions (D2Q9). For the employed D2Q9 LBM, the discrete particle velocity e_i and weighting factors related to the quadrature denoted by w_i are documented in Ref. [43].

One principal approach to mimic this is the linearization of small thermodynamic equilibrium perturbations, known as the single-relaxation-time BGK collision operator. This operator represents the collision term as a linear relaxation toward Maxwellian equilibrium as follows:

$$\Omega_i = -\omega\big[f_i(\vec{x},t) - f_i^{\mathrm{eq}}(\vec{x},t)\big], \tag{2}$$

where ω is the relaxation frequency coefficient. In the Gram-Schmidt MRT collision operator, single relaxation time is replaced by a relaxation time matrix S that relaxes each moment with matrix $M(m = Mf)$ separately. Accordingly, the collision operator for MRT-LBM is as follows:

$$\Omega_i = -M^{-1}S\big[m_i(\vec{x},t) - m_i^{\mathrm{eq}}(\vec{x},t)\big], \tag{3}$$

In Eq (3), the postcollision step is expressed on the right-hand side after being transformed into moment space by the orthogonal matrix M. Using the Gram-Schmidt technique and the D2Q9 lattice model, the matrix M is adopted as documented in Ref. [44]. Here, S is the matrix of relaxation rates and takes on the diagonal form in the Gram-Schmidt basis:

$$\mathrm{S} \equiv \mathrm{diag}(0, \omega_e, \omega_\epsilon, 0, \omega_q, 0, \omega_q, \omega_v, \omega_v). \tag{4}$$

Zero relaxation rates are shown above for the conserved moments of density and momentum. Here, ω_v and ω_e are related to shear and bulk viscosities given by $\mu = \rho c_s^2(\frac{1}{\omega_v} - \frac{1}{2})$ and $\mu_b = \rho c_s^2(\frac{1}{\omega_e} - \frac{1}{2}) - \frac{\mu}{3}$, respectively, and ω_ϵ and ω_q are adjustable parameters.

Here, f_i^{eq} is the equilibrium distribution function and represents the local equilibrium state of the fluid at each lattice node. It evolves the distribution function in time to simulate fluid flow. It is derived from the discrete Boltzmann equation and approximates the statistical behavior of particles in the fluid:

$$f_i^{\mathrm{eq}}(\vec{x},t) = \rho w_i\left[1 + \frac{e_{i\alpha}u_\alpha}{{c_s}^2} + \frac{\left(e_{i\alpha}e_{i\beta} - {c_s}^2\delta_{\alpha\beta}\right)u_\alpha u_\beta}{2{c_s}^4}\right]. \tag{5}$$

The equilibrium moment in the MRT approach $m^{\mathrm{eq}} = \mathbf{M}f^{\mathrm{eq}}$ is calculated based on the equilibrium distribution function f^{eq}.

A Gauss-Hermite quadrature is used to reconstruct macroscopic moments from the Hermite polynomial expansion of f_i on a discrete lattice. The momentum $\rho u = \sum_i f_i e_i$ and density $\rho = \sum_i f_i$, which make up the first two moments of the velocity distribution functions, are conserved moments, and the lattice speed of sound is likewise connected to the quadrature by $c_s = c\frac{\Delta x}{\Delta t}$.

1. Rate of strain and non-Newtonian effective viscosity

Generally, the kinematic viscosity ν is defined as follows in the BGK-LBM framework:

$$\nu = \left(\frac{1}{\omega} - 0.5\right)c_s^2. \tag{6}$$

This relationship can be utilized to calculate the kinematic viscosity of MRT model using the last two relaxation moments of ω_v from the relaxation matrix in Eq. (4). Accordingly, the final expression of the strain rate tensor in the LBM framework for both BGK and MRT collision operators can be obtained as follows [16]:

$$S_{\alpha\beta} = -\frac{0.5}{\rho c_s^2 \delta t}\sum_i e_{i\alpha}e_{i\beta}\Omega_i \tag{7}$$

To determine the strain rate tensor using each collision operator, it is necessary to replace Ω_i with the corresponding collision operators from either the BGK or MRT model, as specified in Eqs. (2) and (3). The assessment of shear rate in these methodologies proves to be highly effective, as it eliminates the need to calculate velocity derivatives. Furthermore, the localized calculation of the shear rate ensures better alignment with the LBM framework. This is especially important when using the numerical solution in a parallel computing environment. Extensive demonstrations have confirmed that this approach, incorporating non-Newtonian effects within the LBM, achieves second-order accuracy [10,37].

We may substitute the $\omega(x,t) = \frac{1}{\tau(x,t)}$ in Eq. (7) to obtain the shear-dependent viscosity of the fluids. Initially, we establish a guess for the relaxation time $[\tau(x,0) = 1]$. Subsequently, we utilize the relaxation times obtained from the prior iteration within Eq. (7) to compute the strain rate tensor.

In a power-law fluid, the shear stress component is given by the constitutive equation of $\tau_{xy} = K\dot{\gamma}^n$, where K is the flow consistency index, $\dot{\gamma}$ is the shear rate, and n is the dimensionless power-law index. The apparent viscosity of the power-law fluid as a function of the shear rate is accordingly given by the following expression:

$$\nu = K|\dot{\gamma}\ |^{n-1}. \tag{8}$$

In Eq. (8), when $n < 1$, the assumption that the power-law behavior persists down to zero shear leads to an infinite viscosity at the limit of zero shear rate ($\dot{\gamma} \to 0$). However, this assumption neglects molecular and structural effects that limit the increase in viscosity as the shear rate tends to zero. To accurately describe the behavior of shear-thinning fluids, we introduce a cutoff limit of $\dot{\gamma}_0 = 10^{-8}$ for zero shear viscosity.

The shear rate $\dot{\gamma}$ is defined using the expression of the second invariant of strain rate tensor as follows:

$$\dot{\gamma} = \sqrt{2\sum_{\alpha,\beta} S_{\alpha\beta}S_{\alpha\beta}}. \tag{9}$$

Consequently, by the combination of Eqs. (6), (8), and (9), the local relaxation frequency can be obtained to calculate local shear-dependent kinematic viscosity in the LBM framework.

2. Flow driving conditions: Body force and pressure

To apply the constant body force term, we utilize the Guo forcing scheme for a constant body force to enhance the accuracy in recovering the Navier-Stokes equations [45]. The Guo forcing scheme calculates the force population during collisions and adjusts the equilibrium and macroscopic velocity fields accordingly. It is well established that the LBM with the Guo forcing scheme can accurately represent the Navier-Stokes equations for Newtonian fluid flows [46]. This scheme involves incorporating an additional term into the right-hand side of the collision operator [Eq. (2)] as follows:

$$F_i = w_i\left(1-\frac{1}{2\tau}\right)\left[\frac{e_i-u}{c_s^2}+\frac{e_i\,(e_i.u)}{c_s^4}\right].F. \tag{10}$$

The actual fluid velocity based on the Gou scheme is defined as follows:

$$u_{\text{real}} = u + \frac{\Delta t F}{2\rho}, \tag{11}$$

where F is the magnitude of the applied force in the horizontal or vertical direction. In the MRT model, one can use a similar form of the force term. Then the relaxed moments using the MRT collision operator [Eq. (3)] become

$$\Omega_i = -M^{-1}S\left[m_i(\vec{x},t) - m_i^{\text{eq}}(\vec{x},t)\right] + \left(1-\frac{S\delta t}{2}\right)MF. \tag{12}$$

The forcing term is initially converted to momentum space using the matrix M. Its influence is then integrated into the corresponding moment by adding it to the collision operator. Following relaxation, the moments are transformed back into population space using $f = M^{-1}m$.

Also, to enforce pressure boundary conditions within our computational framework, we employed the boundary treatments devised by Zou and He [47]. This approach, which applies Dirichlet boundary conditions at both the inlet and outlet, was uniformly adopted for both MRT and BGK models in a same way. The Zou and He boundary condition method effectively applies pressure boundary conditions in LBM simulations by specifying macroscopic quantities such as pressure directly at the inlet and outlet. This is achieved by relating pressure to density using the equation of state $p = \rho c_s^2$, allowing for the adjustment of density at the boundaries to match the desired pressure levels. At these points, the unknown distribution functions, those streaming from outside the computational domain, are recalculated based on the known internal distributions and the specified macroscopic conditions. This recalibration ensures the conservation of mass and momentum at the boundary.

III. RESULTS AND DISCUSSIONS

A. Steady-state power-law Hagen-Poiseuille flow in aligned channel

We first investigate a 2D aligned channel flow using the BGK and MRT collision operators and a halfway bounce-back wall boundary condition. Numerical experiments are based on two distinct scenarios. One scenario is flow driven by a constant body force applied perpendicular to the walls of the channel, while a pressure drop drives the other scenario. Following a grid convergence assessment, detailed later in this paper, the channel width H has been chosen to be 40 l.u., and the channel length is selected to be 120 l.u. The channel accommodates non-Newtonian power-law fluids with various power-law indexes. The Reynolds number for power-law fluid flow is defined as

$$\text{Re} = \frac{u_{\max}^{2-n}H^n}{K}, \tag{13}$$

where $u_{\max}$ represents the maximum velocity attained by the flow at a position $H/2$. In all simulations, the Reynolds number is fixed at a value of $\text{Re} = 10$.

At the point of steady state, the analytical solutions for power-law Hagen-Poiseuille flow driven by uniform body force can be described as follows:

$$u_x(y) = \frac{n}{n+1}\left(\frac{F_x}{k}\right)^{1/n}\left[\left|\frac{H}{2}\right|^{(n+1)/2} - \left|\frac{H}{2}-y\right|^{(n+1)/2}\right]. \tag{14}$$

Simulations were conducted using a flow consistency index of $k = 0.05$ and several power-law index values, including $n = 0.25$, 0.5, 0.75, 1.25, 1.5, and 1.75. These values range from highly shear-thinning behavior to highly shear thickening. The Newtonian assumption of $n = 1$ was also used to assess the accuracy of the solver.

Table I lists the magnitude of forcing values corresponding to various non-Newtonian fluids, all chosen to maintain a constant Reynolds number ($\text{Re} = 10$). Also, Table II presents the pressure drop values to maintain this constant Reynolds number. The following convergence criterion is used to determine the steady-state condition in both cases:

$$\sum_{i,j}\left[u_x(t,y) - u_x(t-\delta t,y)\right] < 10^{-8}. \tag{15}$$

In the channel, the x axis represents orientation parallel to the walls, while the y axis represents orientation perpendicular to the walls. The analytical solution, denoted in Eq. (14), was evaluated along with its first derivative concerning the y positions in the vertical direction of the channel. A comparison was then made between these analytical results and steady-state velocity and shear-rate profiles. The errors were identified by employing the L2 norm of the x-velocity component parallel to the walls:

$$E_{l2} = \sqrt{\frac{\sum_{i,j}\left(u_x^{\text{Analytical}} - u_x^{\text{Numerical}}\right)^2}{\left(u_x^{\text{Analytical}}\right)^2}}. \tag{16}$$

Figure 1 indicates the velocity profiles obtained through analytical solutions and numerical simulations using the MRT collision operator. Results suggest that the simulated data

TABLE I. Force magnitudes across power-law indexes for aligned channel flow at $\text{Re} = 10$.

n	0.6	0.7	0.8	0.9	1.0
F_x	2.3×10^{-4}	1×10^{-4}	2×10^{-4}	6×10^{-5}	1.4×10^{-5}

TABLE II. Pressure drop across power-law indexes for aligned channel flow at Re = 10.

n	0.6	0.7	0.8	0.9	1.0
$p_{\text{inlet}} - p_{\text{outlet}}$	2.66×10^{-2}	1.193×10^{-2}	4.83×10^{-3}	1.6×10^{-3}	3.83×10^{-4}

align excellently with the analytical data, thereby validating the accuracy of the numerical approach by capturing the shear-thinning and thickening behavior of the fluids.

In addition to the comparisons presented for the velocity profiles, Fig. 2 shows excellent agreement between the first derivative of the analytical solution of the velocity profile for power-law fluids and the shear rate obtained from Eq. (9). This further validates the accuracy and reliability of the numerical approach in capturing the nonlinear behavior of the stress-strain rate of the non-Newtonian fluids.

Additionally, various height node numbers (N_y) are employed to scale and evaluate the resolution of the channel grid. The values of N_y are defined by $N_y = H/\delta y$, where δy represents the spacing between the nodes. The specific values used for N_y in this paper are 21, 31, 41, and 51, while $\delta y = 1$. L2 errors acquired from all simulations are presented in Fig. 3 to demonstrate the accuracy of the solver further. Figure 3(a) shows that the numerical model is almost second-order accurate in space for all values of n for velocity. Figure 3(b) also confirms the model is close to second-order accuracy for estimating the shear rate in space.

1. *The influence of the collision operator and non-Newtonian rheology on numerical stability*

Herein, we examine the stability of collision operators for pressure-driven non-Newtonian fluid flows in the aligned channel with $N_y = 21$ l.u. and length of 63 l.u. These models include the BGK model, the Gram-Schmidt MRT model with $\omega_e = \omega_{q,\varepsilon} = 1$ and $\omega_e \neq \omega_{q,\varepsilon} \neq 1$ relaxation parameters. The goal is to determine the maximum nondimensional velocity that could be attained for different nondimensional viscosities and flow consistency indexes. The findings from Newtonian simulations are presented in Fig. 4. The figure demonstrates that using the Gram-Schmidt collision operator expands the stability domain, even without independent control over bulk viscosity and tunable relaxation rates. To determine the relaxation parameters, we conducted a series of simulations across a series of relaxation parameters. Our selection criteria focused on the parameters that showed the greatest stability in both Newtonian and non-Newtonian cases. With unequal relaxation rates $\omega_e = \frac{1}{0.3}$ and $\omega_{q,\varepsilon} = \frac{1}{0.5}$, instabilities stemming from normal modes are further minimized, leading to an expanded stability domain by independently manipulating the bulk viscosity. With low nondimensional viscosities, this extended domain allows for nondimensional velocities as high as 0.4. This demonstrates the justification for using the MRT collision operator.

For Newtonian fluids, having a constant relaxation time while $\frac{1}{\omega} > 0.5$ ensures a positive viscosity value [see Eq. (6)] throughout the simulation domain, regardless of the collision operator used. When dealing with non-Newtonian fluids, introducing the power-law index adds complexity and requires the local adjustment of the relaxation time based on the viscosity of the fluid as a function of shear rate. As the power-law index deviates from unity, the fluid exhibits either shear-thinning or thickening behavior, leading to relaxation time changes. These variations contribute to the gradient of relaxation time and the disparity in fluid particles reaching equilibrium, which can lead to numerical instability. This instability can be observed as unphysical oscillations or a complete breakdown of the simulation. Hence, it is crucial to thoroughly investigate the numerical stability of the non-Newtonian solver using both simple and advanced collision operators to ensure accurate and reliable simulations.

Figure 5 provides a numerical stability analysis over a wide range of flow consistency index. In our experiment, we investigated the behavior of various fluids by adjusting their flow properties. We started by setting the power-law indices n of these fluids within a range from 0.3 to 1.7. We began our measurements with a flow consistency index k of 0.01 for each specific power-law index then gradually increased this index to a maximum of 0.2. We made these adjustments in small increments of 0.01. As we increased the flow consistency index for each fluid, we also slowly raised the pressure

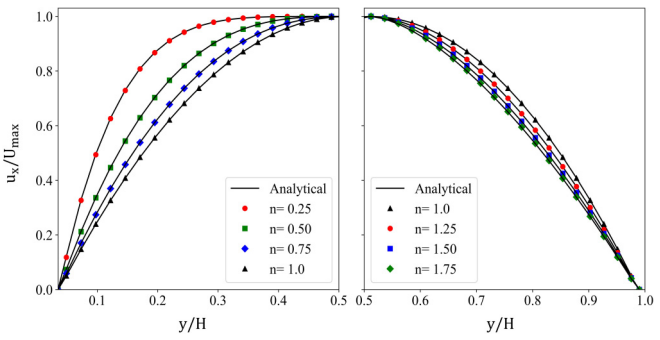

FIG. 1. Comparison between analytical and multiple relaxation time (MRT) velocity profiles of power-law fluid flows with different indices (n) ranging from 0.25 to 1.75 at Re = 10.

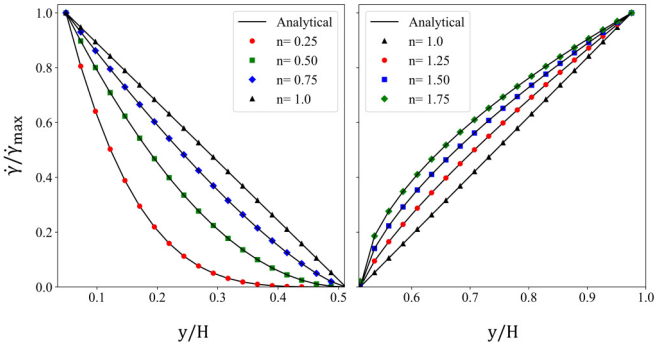

FIG. 2. Comparison between Analytical and multiple relaxation time (MRT) shear-rate profiles of power-law fluid flows with different indices (n) ranging from 0.25 to 1.75 at Re = 10.

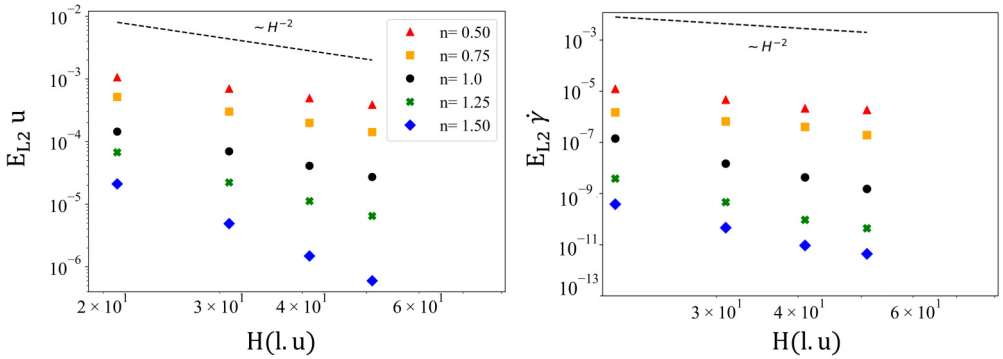

FIG. 3. Scaling behavior of the L2 norm of the global error for the two-dimensional (2D) steady power-law Hagen-Poiseuille flow with different flow indices and Reynolds number (Re = 10). The dashed line indicates second-order convergence in space.

gradient. This stepwise increase in pressure was continued until the point where our simulation could no longer maintain stability. The maximum velocity that could be achieved without the simulation breaking down was recorded for each combination of flow consistency index and power-law index, providing information into the limits of stable flow under varying conditions. To visually represent the results, Fig. 5 presents contour plots that illustrate the impact of varying both the flow consistency index and the pressure gradient on fluid velocity. Approximately 55 000 simulations were systematically performed to generate the detailed data showcased in the plots presented.

The dark blue region signifies the areas where we have reached the peak velocity of $u_{\max} = 0.413$, representing the upper limit of our current simulation capabilities. Conversely, the red regions show zones of instability, where the velocities achieved fall lower than this maximum. In Fig. 5(a), it becomes evident that numerical instabilities arise at very low and very high power-law indices, making it challenging to increase the velocity within the domain without encountering issues. Additionally, the flow consistency index (K) plays a significant role in stability. When selecting low K values, the local relaxation time values approach 0.5, which results in instability. Therefore, to maintain a stable numerical solution using the BGK collision operator, the power-law index should be within the range of 0.48 to 1.66. Furthermore, it is advisable to maintain the flow consistency index within the range of 0.6 to 2 for computational feasibility and stability.

On the other hand, Fig. 5(b) presents the results when incorporating the MRT collision operator without independent control of bulk viscosity and collision frequencies $\omega_e = \omega_{q,\varepsilon} = 1$. Notably, the stability of non-Newtonian simulations is significantly enhanced by using this operator. Solutions approach numerical instability only when the power-law indexes are very low and the flow consistency is high. However, it is essential to note that the maximum achievable velocity in some regions may not reach the maximum value. To overcome this limitation, adjusting the relaxation time of bulk viscosity and other freely adjustable relaxation parameters independently proves to be effective.

For the specific relaxation rates selected ($\omega_e = \frac{1}{0.3}$ and tunable relaxation parameter of $\omega_{q,\varepsilon} = \frac{1}{1.7}$), the results are shown in Fig. 5(c). It becomes evident that the instability regions are limited to very low power-law indices and high flow consistency indices. Therefore, it is appropriate to implement the MRT collision operator with the tuning of relaxation parameters to ensure a stable numerical solution for non-Newtonian flows. Regrettably, the existing literature does not provide guidelines or systematic relations for selecting suitable relaxation values for various fluids. Later in this paper, we will address this gap by discussing the selection based on the physical characteristics of non-Newtonian LBM.

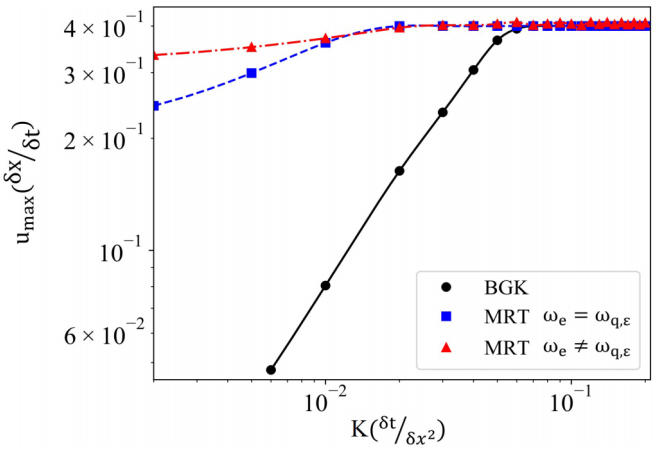

FIG. 4. Stability domains using a D2Q9 stencil Bhatnagar-Gross-Krook (BGK; black circles), multiple relaxation time (MRT) with $\omega_e = \omega_{q,\varepsilon}$ (blue squares), and MRT with $\omega_e \neq \omega_{q,\varepsilon}$ (red triangles).

2. Optimal consistency index for bounce-back resting walls

Lattice Boltzmann link-wise boundary conditions are subject to distinct closure rules that differ from those applied to the bulk. Consequently, expecting the macroscopic bulk behavior to remain consistent at the boundaries is unreasonable. According to earlier studies, the bounce-back scheme in a unidirectional Newtonian Poiseuille flow, confined between two infinite flat plates, can result in minor hidden errors such as slip velocity [22]. Through Chapman-Enskog analysis, it has been established that the dynamic viscosity (μ) of the simulated fluid is intrinsically linked to the relaxation time.

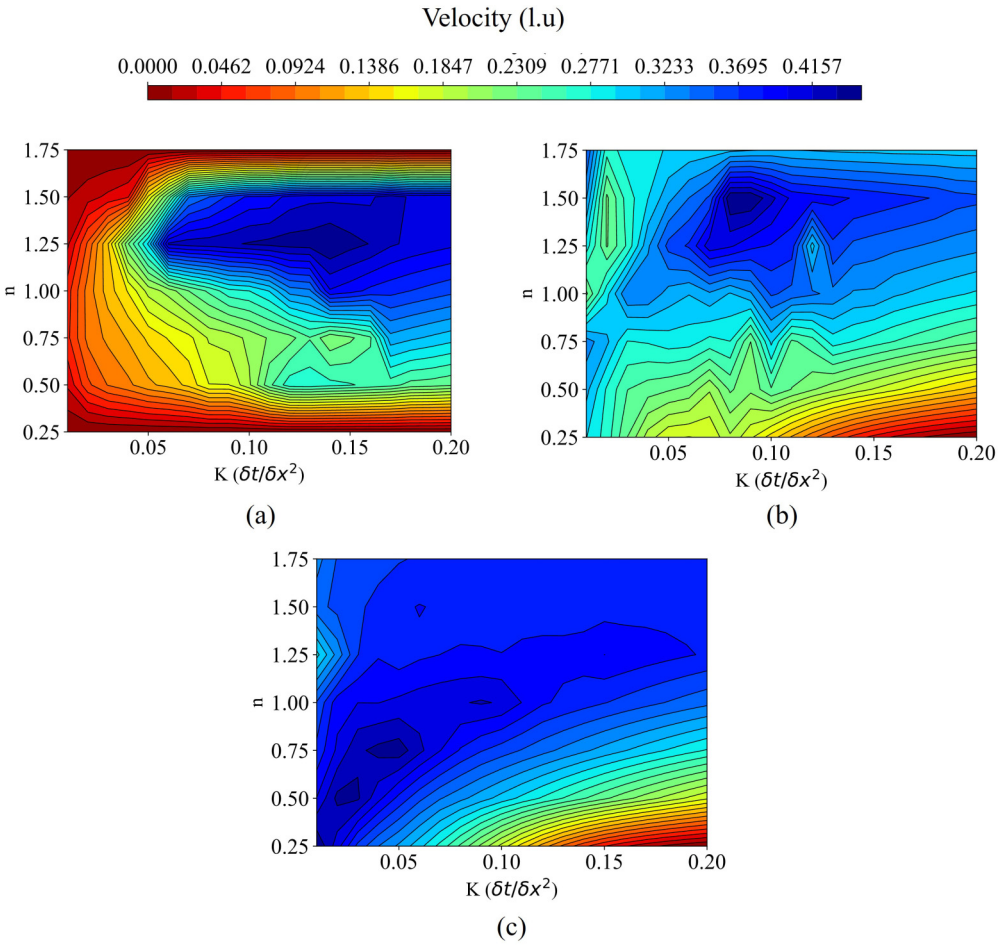

FIG. 5. Stability domains of the highest reachable velocity of the non-Newtonian solver are illustrated in blue. (a) Bhatnagar-Gross-Krook (BGK) collision operator, (b) multiple relaxation time (MRT) with $\omega_e = \omega_{q,\varepsilon}$, and (c) MRT with $\omega_e \neq \omega_{q,\varepsilon}$.

This underscores that any alteration in the relaxation time within the BGK model will directly influence the viscosity of the simulated fluid. As a result, an explicit and inherent dependency exists between the relaxation time and viscosity when the BGK model is employed. In the simulation of Newtonian fluid dynamics using the BGK collision operator combined with the bounce-back scheme, it has been found that, for choosing relaxation time, only when the relation $(\tau - \frac{\delta t}{2})^2 = \frac{3}{16}$ is satisfied can the exact parabolic solution of the Hagen-Poiseuille flow be achieved. This optimal value is derived from a detailed mathematical process of the Chapman-Enskog expansion [48]. In this context, setting the relaxation time τ according to the formula aligns the behavior of the simulated fluid using LBM with the Navier-Stokes equations. In the case of non-Newtonian power-law fluids, the relaxation time is no longer constant and is instead dependent on the shear rate and flow consistency index, which complicates the mathematical expression of Chapman-Enskog analysis for obtaining the optimal relaxation time. When the fluid is Newtonian, kinematic viscosity corresponds to a flow consistency index of K. Thus, regarding the optimal relaxation formula, the optimal flow consistency index for Newtonian fluids can be obtained as $K \approx 0.1443$. Herein, we conducted systematic numerical experiments using a Poiseuille flow setup designed for force-driven flows. We varied the power-law indices of the fluids between $n = 0.6$ and 1.4. For each, starting with a flow consistency index of 0.01, we incrementally increased it up to 1, using steps of 10^{-4}. The outcomes of these experiments are illustrated in Fig. 6(a), which presents the results for relative error values of velocity profiles for shear-thinning fluids. It can be observed that the optimal consistency index for these fluids is lower than that for Newtonian fluids, indicating a backward shift with the decrease in the power-law index. On the other hand, Fig. 6(b) shows the relative error values for shear-thickening fluids. Here, an increase in the optimal flow consistency index can be seen as the power-law index is increasing.

In the numerical experiments, it was observed that increasing the flow consistency index for shear-thinning fluids led to elevated relaxation times and viscosities in low-shear regions. Accordingly, higher k values resulted in overrelaxation, which is associated with numerical errors in BGK-LBM, particularly when the power-law index was decreased. Consequently, it is essential to keep K below the Newtonian limit to minimize such errors while accommodating varying power-law indices. Conversely, in the case of shear-thickening fluids, lowering the flow consistency index reduced relaxation times and viscosities in low-shear regions, approaching the stability

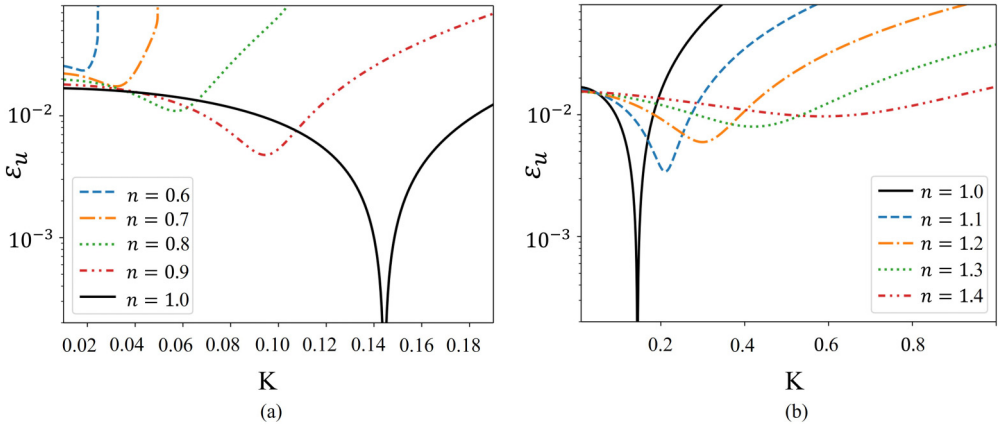

FIG. 6. Systematic study of flow consistency index (K) on minimal error value of unidirectional flow for (a) shear-thinning and (b) shear-thickening fluids along with a Newtonian assumption.

limit of the LBM ($\tau = 0.5$), which caused underrelaxation. To maintain simulation stability and avoid small relaxation time values, it is evident that selecting higher k values relative to the Newtonian limit is necessary.

In Newtonian fluids, by choosing optimal relaxation time, the BGK-LBM simulation results align perfectly with the parabolic solution of the Hagen-Poiseuille flow, limited only by machine precision. This level of precision is not attainable with non-Newtonian fluids due to their more complex flow and LBM characteristics. However, we can achieve the lowest possible error rates in our simulations by accurately determining the optimal flow consistency index for different types of non-Newtonian fluids.

Through detailed analysis of the minimum error values associated with each power-law index and its corresponding flow consistency index, it is possible to derive an expression representing the optimal flow consistency index as a function of the power-law index. This relationship is graphically depicted in Fig. 7. Observations reveal that the flow consistency and power-law indexes are interconnected through a nonlinear relationship. By applying a power fitting to the data, this relationship can be formulated in a mathematical expression presented as Eq. (17). Utilizing this formula to simulate non-Newtonian power-law fluid flows can help minimize errors in selecting the ideal flow consistency index when using the BGK collision operator and bounce-back boundary conditions:

$$K(n) = K_{\text{Newtonian}}(n)^{4.1}, \tag{17}$$

where $K_{\text{Newtonian}} = \frac{\sqrt{3}}{4}$ is the optimal flow consistency index for Newtonian assumption. Figure 8 showcases a series of numerical experiments investigating velocity profile errors for a diverse range of non-Newtonian fluid flows using an MRT collision operator with $\omega_\gamma = 1$. These flows have varying power-law indices and flow consistency indices. In this context, there is no optimal relaxation time to prevent slip velocity, and the MRT approach effectively addresses the viscosity dependence of the bounce back. The results indicate

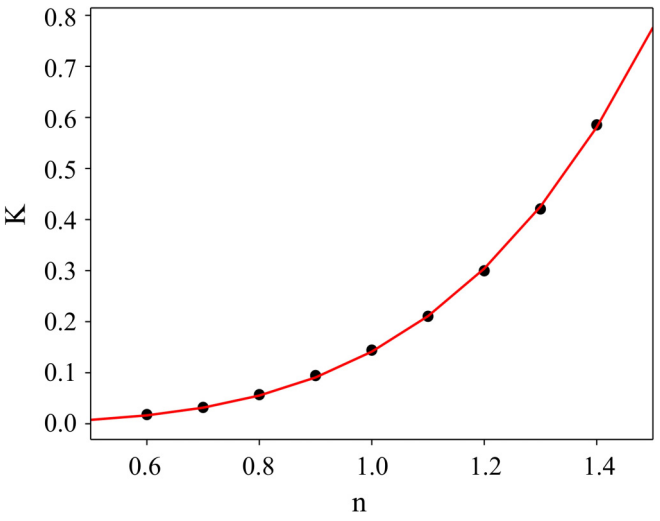

FIG. 7. The behavior of optimal flow consistency index (K) as a funtion of power-law index.

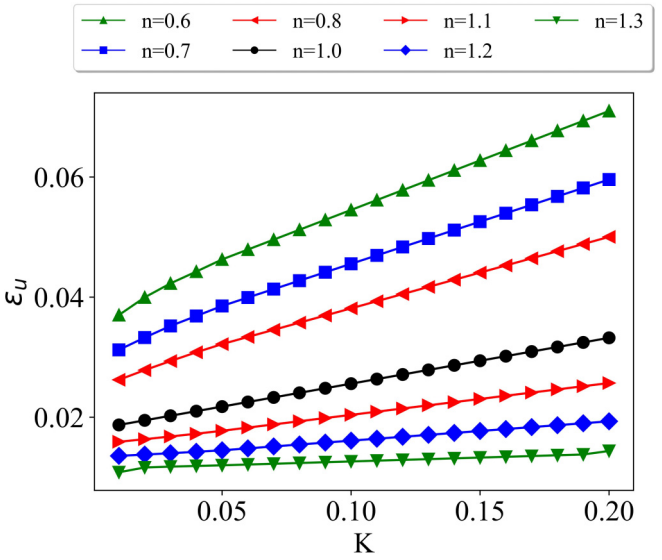

FIG. 8. Comparison of non-Newtonian MRT-LB, solver for velocity profile errors for various flow consistency and power-law indexes (range $= 0.6 \leqslant n \leqslant 1.3$).

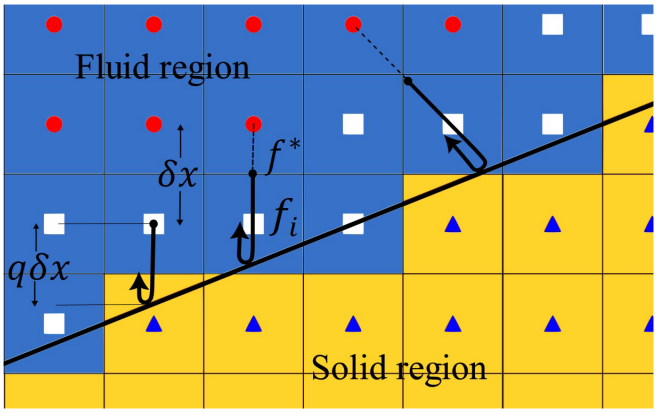

FIG. 9. Schematic of linear interpolated bounce back in an inclined channel.

that the error values increase with higher flow consistency indices, and this increase is particularly pronounced in the case of shear-thinning fluids. Consequently, the crucial aspect to consider using the MRT approach is maintaining the flow consistency index within the stability region to prevent the growth of errors.

B. Steady-state power-law Hagen-Poisseuile flow in inclined channel

To investigate the properties of the non-Newtonian LBM and WSS considering stair-shaped walls, we first conduct numerical experiments in a 2D inclined channel setup driven by constant body force and then pressure-driven titled channel flows, respectively. This setup involves parallel walls inclined at an angle θ relative to the lattice axis. To simulate the behavior of non-Newtonian fluids accurately, we utilize the LBM with IBB boundary treatment and employ both BGK and MRT collision operators. In the IBB approach, a boundary link typically intersects the physical wall at a specific distance since the wall is not situated precisely halfway between lattice nodes and cannot reach another lattice node directly. Consequently, the origin of the population is selected to ensure the exact reaching of a lattice node by the corresponding fraction. This necessitates the use of interpolation to determine the postcollision value of f_i, as depicted in Fig. 9. A parameter q is used to describe the fraction of an intersected connection inside the fluid zone as

$$q = \frac{|r_{\text{boundary}} - r_{\text{fluid}}|}{|r_{\text{solid}} - r_{\text{fluid}}|}. \tag{18}$$

Figure 9 depicts the boundary, fluid, and solid node arrangement of an inclined channel. In this representation, boundary nodes, denoted by square symbols, are located within the fluid region; fluid nodes are represented by circle symbols; and solid nodes are denoted by triangle symbols. The solid line represents the physical wall. By employing these definitions, one can calculate the distance fraction q. Using linear interpolations based on distance fractions, we can construct a bounce-back population that was previously unknown from the known postcollision populations. The general algorithm for implementing this linear IBB is as follows [18]:

$$f_{\bar{i}}(x_b, t + \Delta t) = \begin{cases} 2q f_i^*(x_{\text{boundary}}, t) + (1 - 2q) f_i^*(x_{\text{fluid}}, t), & q \leqslant \frac{1}{2}, \\ \frac{1}{2q} f_i^*(x_{\text{boundary}}, t) + \frac{2q-1}{2q} f_{\bar{i}}^*(x_{\text{solid}}, t), & q > \frac{1}{2}. \end{cases} \tag{19}$$

In the LBM framework, WSS measurements are typically derived from the location and orientation of the boundary. These measurements can be locally calculated using the distribution functions and the Einstein summation convention:

$$\tau_{\text{WSS}} = \sigma_{\alpha\beta}\hat{n}_\beta - (\sigma_{\beta\gamma}\hat{n}_\beta\hat{n}_\gamma)\hat{n}_\alpha, \tag{20}$$

where viscous stress $\sigma_{\alpha\beta}$ is proportional to strain rate S:

$$\sigma_{\alpha\beta} = 2\mu S_{\alpha\beta}. \tag{21}$$

As a standard practice for WSS measurements, the magnitude of the WSS vector is often focused on disregarding the subtracted normal component in Eq. (20) that contributes to the wall pressure. However, this approach is based on the fact that, due to mass conservation, the fluid velocity should have no component perpendicular to the wall at any point along the wall. Therefore, it is expected that the relationship $n_\alpha u_\alpha = 0$ holds precisely at every wall position. It is important to note that this conservation may not be maintained in the IBB due to mass imbalance caused by interpolations.. Furthermore, when considering curved walls, it is observed that certain situations arise where a section of the wall is parallel to discrete lattice velocity directions. In such cases, the errors resulting from the projection of normal vectors tend to be smaller than other angles and directions [25]. The inaccuracies introduced by the stair-step approximation and wall roughness are eliminated when the wall is parallel to the lattice directions. On the other hand, when dealing with directions that are not parallel to lattice Boltzmann directions, the calculations of normal vectors introduce errors, indicating a dependence on the orientation of the walls. Accordingly, instead of directly calculating WSS on the wall, we focus on determining the magnitude of local shear stresses and their distribution on the fluid nodes closest to the solid wall:

$$\tau_{\text{WSS}} = \mu(x)\dot{\gamma}(x), \tag{22}$$

where $\mu(x)$ and $\dot{\gamma}(x)$ are local dynamic viscosity and shear rate on fluid nodes adjacent to solid boundaries.

1. *Force-driven power-law fluid flow in tilted channels*

First, we apply a force within this framework to drive the flow along the inclined channel with periodic inlet and outlet boundary conditions. By varying the inclination ratio θ, we investigated the impact of channel inclination on the flow

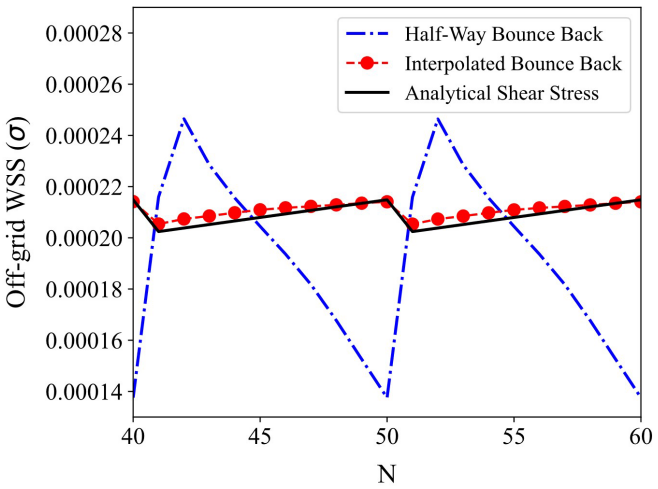

FIG. 10. Shear stress distribution comparison of Newtonian fluid flow ($n = 1$) at the nearest node to the physical boundary using Bhatnagar-Gross-Krook (BGK) collision operator, $\theta = 0.1$, and $\mathrm{Re} = 10$ with analytical solution.

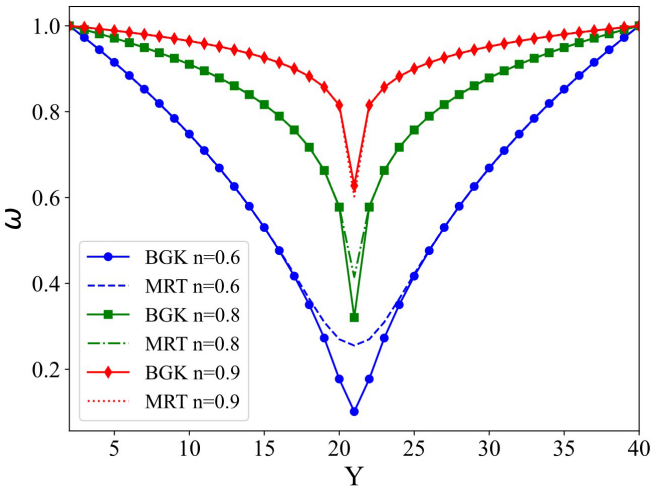

FIG. 11. Comparison of local collision frequencies in three shear-thinning fluids: Bhatnagar-Gross-Krook (BGK) vs multiple relaxation time (MRT) methods.

behavior and the resulting distribution of WSS in complex rheology of non-Newtonian fluids. To ensure a consistent comparison, we employed laminar flow conditions and maintained a constant value of $\mathrm{Re} = 10$ across all experimental conditions. For the inclined channel configuration, we selected a channel width of $N = 30$, and the channel length was set to be three times longer than the width. To ensure a consistent number of fluid nodes ($N_f \approx 3000$) we adjusted the domain size for all inclinations and flow conditions. This approach allowed us to ensure consistent resolutions for all inclinations and flow conditions.

Figure 10 compares the Newtonian fluid WSS distributions obtained from the BGK collision operator with the halfway bounce-back and IBB techniques. The analysis focuses on the closest fluid nodes to the wall along 20 nodes in the x direction, with a specific consideration of $\theta = 0.1$ and $\mathrm{Re} = 10$. Evidently, the halfway bounce-back and staircase approximations deviate from the analytical solution. This discrepancy arises due to the neglect of wall smoothness in the staircase model, resulting in high- and low-shear regions due to the wall roughness and flow over the steps. Conversely, the IBB approach restores wall smoothness effectively and yields a more accurate distribution of WSS along the inclined channel.

We explore advanced collision operators to restore non-Newtonian shear-dependent viscosity, considering the unique characteristics of the BGK and MRT operators. In our numerical experiments, we observed that using the MRT method when dealing with Newtonian fluid flows did not result in significant improvement beyond achieving numerical accuracy. However, when simulating non-Newtonian fluid flows, we observed a variation in the local relaxation time, corresponding to the kinematic viscosity and making a significant difference. Section III B discussed that the MRT collision operator demonstrates better stability than the BGK collision operator across a wide range of flow consistency indices. This enhanced stability is particularly evident in shear-thinning fluids, where the kinematic viscosity is higher in low-shear regions, increasing the local relaxation time. Consequently, the MRT method is expected to exhibit higher numerical stability than the BGK collision operator in these regions of low shear.

Figure 11 illustrates the local collision frequency incorporated into the BGK and MRT collision operators for three different shear-thinning fluids under the same flow conditions along the vertical direction of the channel y. This figure shows that both operators behave similarly in regions of high-shear rates when recovering collision frequency. However, they display differences in low-shear-rate regions. As the power-law index approaches the Newtonian limit, the deviations diminish, and the differences between MRT and BGK become more noticeable in highly shear-thinning fluids and low-shear regions.

Herein, we conduct numerical experiments to assess the viscosity dependence on mass conservation in non-Newtonian simulations. Figure 12 illustrates a series of simulations in an inclined channel with $\theta = 0.25$, periodic inlet and

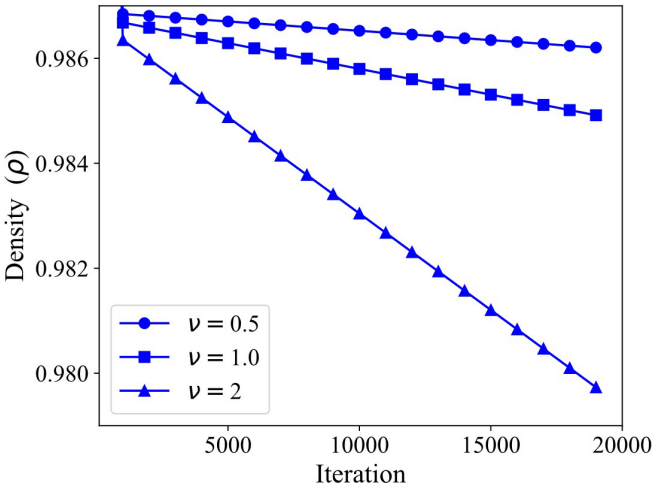

FIG. 12. Mass imbalance in an inclined periodic channel with Newtonian force-driven flow ($n = 1$, $\theta = 0.25$, $\mathrm{Re} = 10$) with different kineamtic viscosities.

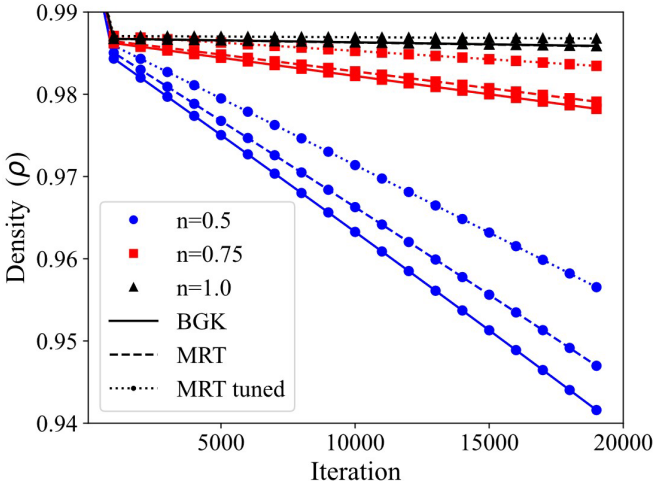

FIG. 13. Temporal evolution of mass imbalance for power-law fluids with $n = 0.5$, 0.75, and 1. A comparison using Bhatnagar-Gross-Krook (BGK), multiple relaxation time (MRT), and tuned MRT collision operators. Simulations were conducted at Re = 10, $\theta = 0.25$, and driven by a constant body force.

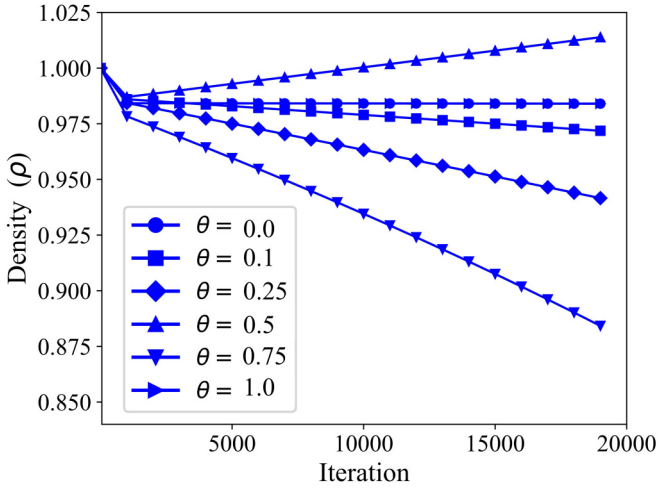

FIG. 14. Temporal evolution of mass imbalance for a power-law fluid with $n = 0.75$ using Bhatnagar-Gross-Krook (BGK) collision operator. Simulations were conducted at Re = 10 and driven by a constant body force.

outlets, two distinct shear-thinning fluids, and a Newtonian fluid ($n = 0.5$, 0.75, and 1). We employed both BGK and MRT collision operators with different relaxation parameters ($\omega_v = \omega_\gamma$ and $\omega_v \neq \omega_\gamma$). From Fig. 12, it can be observed that, as the kinematic viscosity increases in Newtonian simulations, the fluid flow experiences a more significant mass loss over time.

In periodic systems with force-driven flow, highly shear-thinning fluids experience a more significant mass imbalance due to their higher viscosity near the boundaries (Fig. 13). Therefore, it becomes crucial to consider special treatments to recover lost or gained mass in such simulations. We also examined the mass conservation of this scenario using the MRT collision operator, considering both tuned and untuned relaxation parameters. By independently adjusting the free relaxation parameters, separate from the local kinematic viscosity, it is possible to modify the distribution functions during the collision process. This, in turn, can have an impact on mass imbalance. By selecting $\tau_b = 0.3$, which represents the stability limit, we can improve the mass balance compared with $\tau_b = 1$. This effect is more pronounced in highly shear-thinning fluids and becomes insignificant for fluids with higher power-law indexes. Consequently, when there is a variation in viscosity in non-Newtonian fluid flows, it is evident that the interpolation of bounce-back wall boundaries can introduce a source of error.

Figure 14 demonstrates the evaluation of a single shear-thinning fluid ($n = 0.75$) under the same flow conditions (Re = 10) but with different inclinations. The mass imbalance of a shear-thinning fluid is highly dependent on the inclinations of the channels and the distance ratios (q) of the corresponding channel inclinations. Accordingly, the local mass imbalance of a periodic system is expected to be highly affected by the variation of numbers and length of stairs of the defined tilted channel. In other words, it is expected to be affected by the degree of misalignment with the lattice and the channel length. In all conditions, except when $\theta = 0.5$, there is a mass imbalance resulting in a mass loss during 20 000 iterations. This could significantly impact the velocity profiles and WSS distributions of a non-Newtonian fluid flow solver.

Figures 15(a) and 15(b) display contoured plots showcasing the velocity profile errors for the MRT and BGK collision operators, respectively. These errors are analyzed concerning two parameters: the power-law index (n) and the inclination angle (θ) channel. Width, length, and Re = 10 are fixed in all simulations. In regions of low shear, the BGK and MRT collision operators show contrasting gradients in local relaxation time, which leads to differences in achieving the desired power-law viscosity and results in variations in velocity profiles. The error differences between the MRT and BGK methods decrease as the power-law index approaches Newtonian fluid. With the Newtonian assumption, no significant disparities are observed, and the MRT collision operator shows more accuracy than the BGK collision operator for simulating shear-thinning fluids.

When $\theta = 0$ or 1, the walls are parallel to the lattice discrete velocity directions, with minimal errors. In the Newtonian limit, the error rate in the velocity profile is a function of the inclination angle and increases as the angle θ increases. However, it can be observed that, by decreasing the power-law index, the error in velocity profiles fluctuates for both BGK and MRT collisions with variations in θ. In cases with more complex wall boundary conditions, mass conservation depends on the inclination of the wall and the power-law index, as discussed earlier. Generally, it was observed that the non-Newtonian LBM produces lower velocities than the analytical solution.

Consequently, a mass imbalance, such as losing or gaining mass, can increase or decrease the velocity of the fluid flow. By decreasing the power-law index and enhancing the shear-thinning effects, the variation of channel inclination affects mass conservation. In the case of $\theta = 0.5$, when additional mass is added to the system, the velocity increases and the velocity profiles become closer to the analytical solution, resulting in a better match, while in other conditions, losing

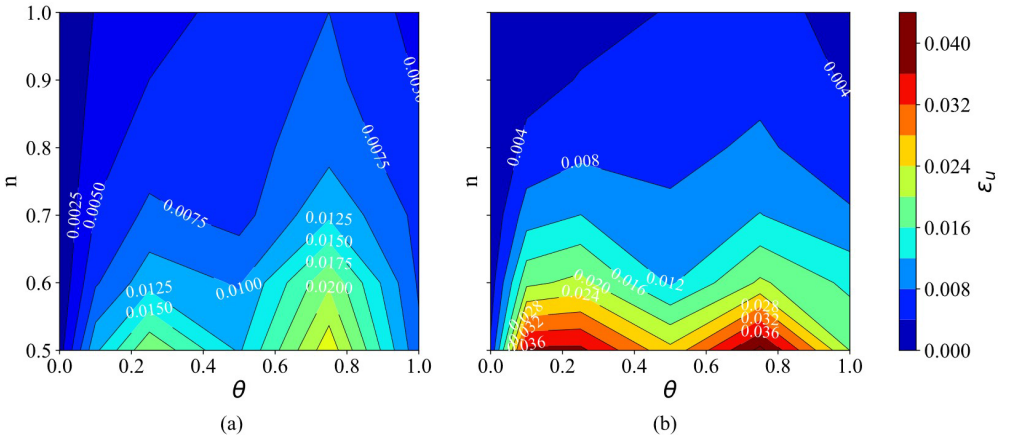

FIG. 15. Conture plots of velocity profile errors as a function of channel inclination (θ) and power-law index (n) using (a) multiple relaxation time (MRT) and (b) Bhatnagar-Gross-Krook (BGK) collision operators.

mass leads to a reduction in velocity in the system and an increase in error.

We observed that the source of error in BGK and MRT collision operators generally could be from the low-shear-rate regions and higher-shear regions like WSS, which can be affected by these numerical characteristics.

Here, we analyze the WSS for these collision operators. Figures 16(a) and 16(b) demonstrate the WSS distribution errors as a function of the power-law index and channel inclinations θ for MRT and BGK collisions. Like velocity profile errors, WSS errors have no significant differences in BGK and MRT collision operators for Newtonian simulations. However, by introducing non-Newtonian effects and increasing the shear-thinning effects, MRT performs more accurately. In Fig. 16, the WSS distribution simulations in highly shear-thinning fluids show fewer errors than the analytical solution under the same flow conditions.

In the previous simulations, we maintained constant Reynolds numbers. Next, we applied a fixed value of body force ($F = 10^{-5}$) to all fluids. In this context, when observing Fig. 17, it becomes evident that the error rate of velocity of the fluid with $K = 0.05$ for highly shear-thinning fluids is significantly higher. Consequently, the WSS distributions encounter higher errors in highly shear-thinning fluids. However, it is apparent that both the MRT and BGK collision models behave similarly as they approach the Newtonian fluid limit. Nevertheless, MRT outperforms BGK in accuracy when dealing with shear-thinning fluids.

The reason behind the higher errors observed in highly shear-thinning fluids when using the BGK collision operator is as follows: In such fluids, the fluid velocity is very low, causing the solution to converge to the convergence criterion rapidly. Due to this swift convergence, the solver has insufficient time for mass imbalance throughout the system. Consequently, this very low velocity can increase velocity error oscillations and a higher error rate.

2. *Pressure-driven power-law fluids flow in tilted channels*

In this section, we aim to explore pressure-driven flows with different non-Newtonian fluid flows. By comparing the results obtained from pressure-driven flows to those from force-driven flows, we can identify the distinctive effects of pressure boundaries and gain insights into the role of pressure

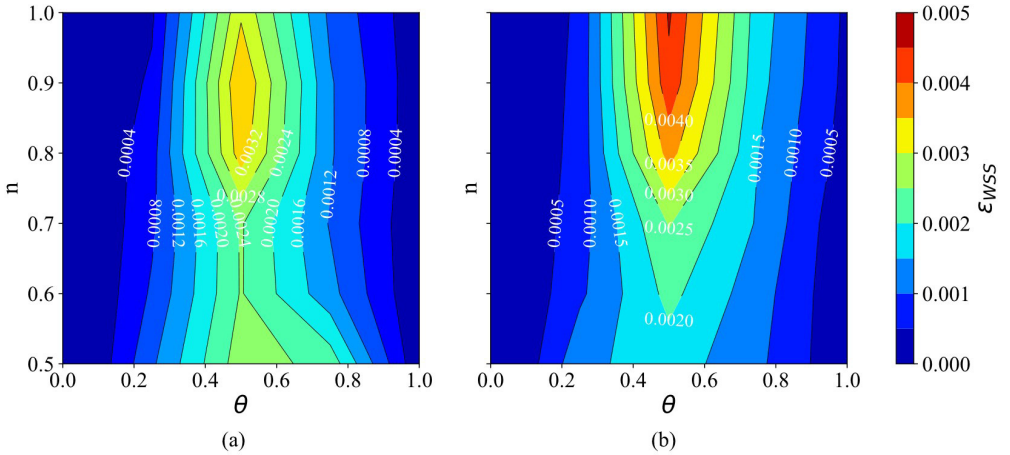

FIG. 16. Conture plots of wall shear stress (WSS) distribution errors as a function of channel inclination (θ) and power-law index (n) using (a) multiple relaxation time (MRT) and (b) Bhatnagar-Gross-Krook (BGK) collision operators. Simulations conducted in constant Reynolds number (Re = 10).

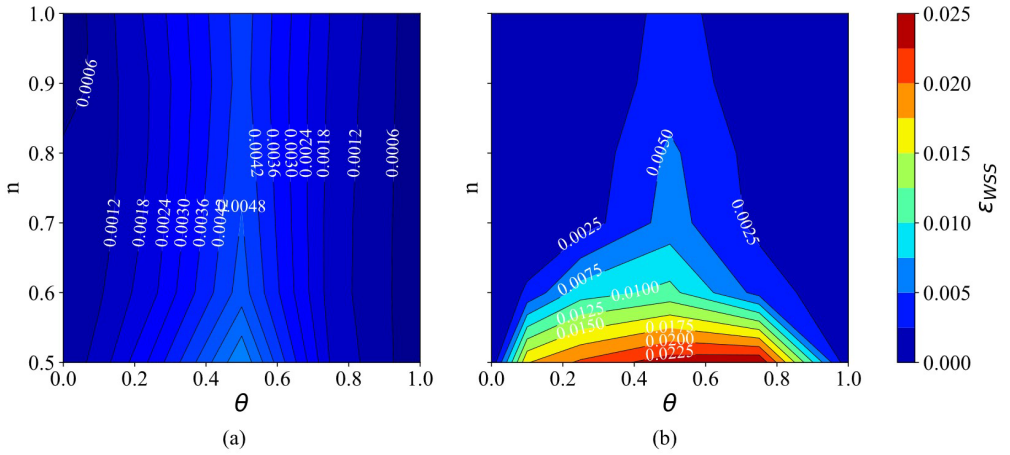

FIG. 17. Conture plots of wall shear stress (WSS) distributions as a function of channel inclination (θ) and power-law index (n) using (a) multiple relaxation time (MRT) and (b) Bhatnagar-Gross-Krook (BGK) collision operators. Simulations conducted in constant body force ($F = 10^{-5}$).

drop in these flows and other independent components of relaxation moment, such as bulk viscosity.

The results in Fig. 18 depict the shear rate of Newtonian and a non-Newtonian fluid ($n = 0.5$) for pressure-driven flow in an aligned channel with the same geometry as discussed earlier and Re = 10. For implementing pressure boundary conditions in a tilted channel, consider using a directional approach to the geometry of the channel. Start by aligning the inlet boundary nodes precisely along a line perpendicular to the actual boundary, reflecting the specific inclination angle of the channel. The pressure of each node is then determined based on its distance from the actual inlet boundary. This setup ensures that the pressure gradient is consistently applied in the direction parallel to the tilt of the channel, and the flow naturally conforms to the angular disposition of the channel. There are no significant differences between MRT and BGK collision operators in the Newtonian limit. By decreasing the power-law index and introducing shear-thinning effects, deviations between these two collision operators can be observed. In this case ($n = 0.5$), when the bulk viscosity (τ_b) is set to 1, no significant differences can be observed compared with simulations using the BGK collision operator. However, adjusting the bulk viscosity in this case to a value of $\tau_b = 0.00925$ corrects the deviation of the shear-rate profile in high-shear regions.

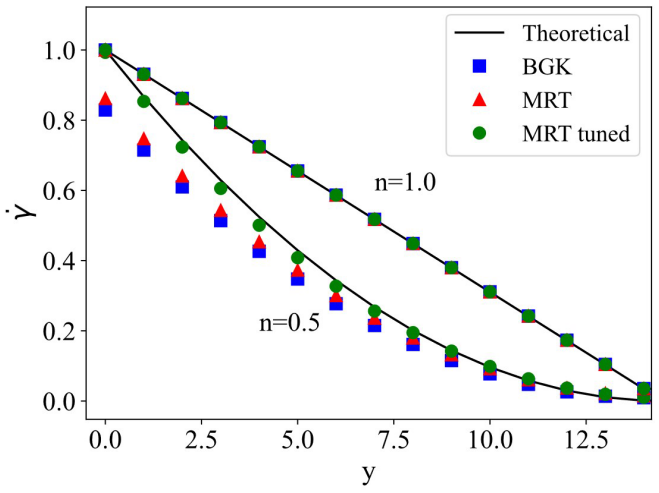

FIG. 18. Comparison of shear-rate profiles of Newtonian and a non-Newtonian fluid ($n = 0.5$) for pressure-driven flow in an aligned channel with Re = 10 using Bhatnagar-Gross-Krook (BGK), multiple relaxation time (MRT), and tuned MRT collisions.

Therefore, we conducted a series of numerical experiments to determine the optimal relaxation times for bulk viscosity. For each shear-thinning fluid, we conducted systematic simulations based on analytical solution values to investigate the control of bulk viscosity to mitigate compressibility effects within the framework of the non-Newtonian LBM. For this, we systematically repeated each simulation based on the error values and the bisection method to minimize the error until the desired error of the velocity profile $\varepsilon_u < 10^{-6}$ was reached. Upon establishing a baseline error, the relaxation time was adjusted by halving, followed by a resimulation to evaluate the impact of this adjustment on the error magnitude. This process was repeated, and if the error was reduced, the relaxation time was further halved; if not, adjustments were made in the opposite direction based on the previous relaxation value. This iterative refinement continued until the error in the velocity profile was reduced below the threshold of $\varepsilon_u < 10^{-6}$, ensuring each step progressively enhanced the accuracy of the fluid dynamics simulation. This bisection approach efficiently converged to the optimal relaxation time. It provided a clear framework for systematically minimizing simulation errors, which is crucial for accurately capturing the complex behavior of non-Newtonian shear-thinning fluids. Our findings revealed that the relaxation of bulk viscosity in the MRT collision operator follows the curve depicted in Fig. 19. This leads to enhanced accuracy while ensuring stability in simulating the flow of non-Newtonian power-law fluids. In highly shear-thinning fluids ($n < 0.6$), the viscosity decreases rapidly as the shear rate increases. Setting a small relaxation time for bulk viscosity is suitable in such cases. A shorter relaxation time allows the fluid to quickly adjust to changes in shear rate, enhancing the ability of the simulation to capture rapid

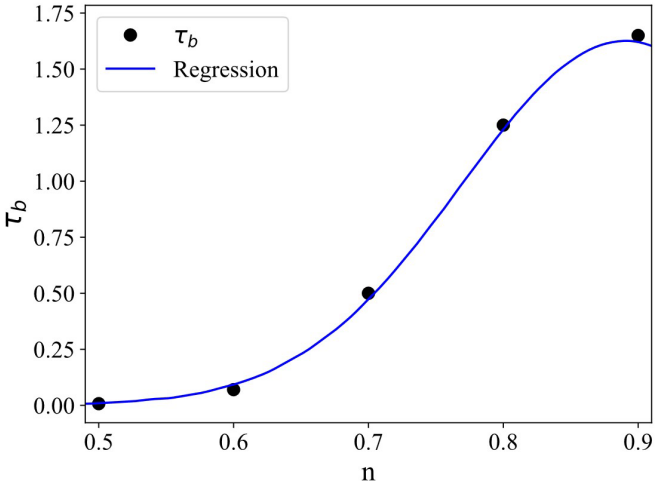

FIG. 19. Gaussian regression of the optimal bulk viscosity relaxation time τ_b as a funtion of power-law index.

TABLE III. Constant parameters used in Eq. (23) to define the best-fitting curve for τ_b value vs n.

	Fitted value	Confidence bound
a	1.654	1.572–1.736
b	0.8909	0.8673–0.9129
c	0.1716	0.1456–0.1978

variations in viscosity and accurately depict shear-thinning behavior. Conversely, for fluids with a power-law index $n \sim 1$, the viscosity exhibits relatively less sensitivity to the shear rate, resembling that of a Newtonian fluid. In this scenario, setting the relaxation time for bulk viscosity too small may lead to inaccuracies. To address this, a longer relaxation time enables the fluid to retain its viscosity for extended durations, effectively mitigating viscosity fluctuations caused by the discrete nature of the LBM. As a result, this approach enhances the accuracy of the simulation when dealing with behavior that is close to Newtonian.

To further evaluate and systematically analyze the results across different Reynolds numbers, we conducted Gaussian regression on the tested relaxation data for Re = 10, as depicted in Fig. 19. We used Gaussian regression since the relaxation time seems to perform a Gaussian evolution with increasing the power-law index. This regression helped us validate and refine our approach, providing insights into the impact of relaxation times on various fluid flow conditions.

The general Gauss regression obtains the following relaxation for the bulk viscosity relaxation time as a function of the power-law index:

$$\tau_b(n) = ae^{[(b-n)/c]^2}. \tag{23}$$

The variables a, b, and c are represented in Table III.

The application of the fitted bulk viscosity relaxation in various flow conditions is presented in Fig. 20. This figure shows the WSS distribution error values and how incorporating Eq. (23) improves the accuracy. The results indicate that errors in WSS become more significant as the power-law

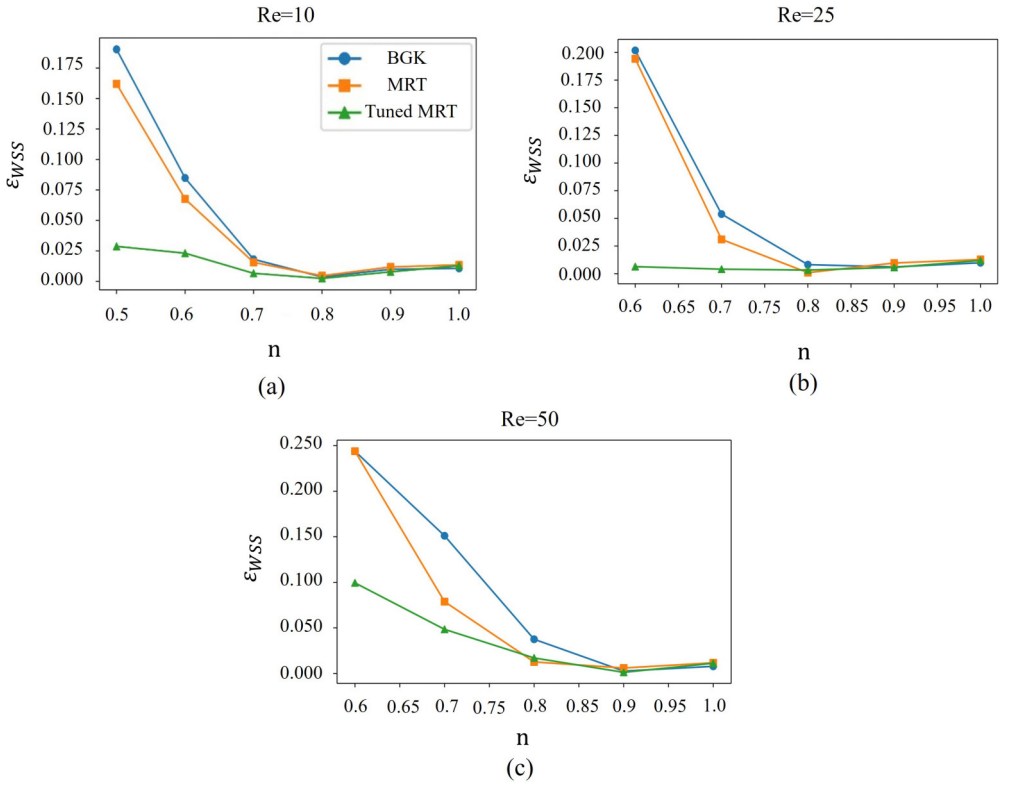

FIG. 20. Comparison of wall shear stress (WSS) errors for (a) Re = 10, (b) Re = 25, and (c) Re = 50 using Bhatnagar-Gross-Krook (BGK), multiple relaxation time (MRT), and tuned MRT collision operators.

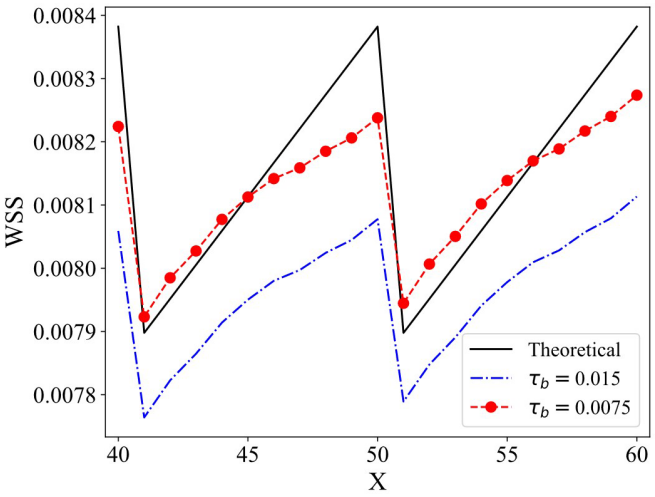

FIG. 21. Analysis of analytical wall shear stress (WSS) distributions along 20 nodes for a highly shear-thinning pressure-driven flow at $n = 0.5$, Re $= 10$, and $\theta = 0.1$ using the multiple relaxation time (MRT) collision operator with variation of τ_b.

index decreases. However, by utilizing Eq. (23), errors caused by rapid variations in viscosity can be effectively minimized. To assess the suitability of the fitted equation across various flow conditions, we tested three distinct Reynolds numbers (Re $= 10,\ 25,$ and 50). Figure 20 demonstrates the significant influence of choosing the correct relaxation time for bulk viscosity on the flow of non-Newtonian fluids at all Reynolds numbers investigated. This impact is particularly pronounced in highly shear-thinning fluids. As the power-law index increases, the effect diminishes until no significant differences are observed in Newtonian fluid flows ($n = 1$). When the Reynolds number and flow velocity are increased, the relative errors in the distribution of WSS also increase. Additionally, as the power-law index decreases and shear-thinning effects become more pronounced, the errors in WSS for both BGK and MRT collision operators rise. However, applying Eq. (22) to the MRT collision for bulk viscosity tuning shows that these error values can be minimized.

Figure 21 compares the analytical WSS distributions for a highly shear-thinning pressure-driven flow at $n = 0.5$, Re $= 10$, and $\theta = 0.1$ using the MRT collision operator over 20 nodes adjacent to the physical wall. Using Eq. (23), we observe that it effectively manipulates the WSS distributions, matching them closer to the analytical solution. When choosing a value twice the amount obtained using the fitted equation, the WSS distributions significantly deviate from the analytical solution. However, it is noteworthy that the accuracy varies at different points. This variation is attributed to the distance of the fluid node, which is considered the closest to the physical wall. As anticipated, at $x = 50$, we expect to see higher errors, as it is the closest point to the physical wall.

Table IV presents the calculated WSS distribution error values at 10 nodes near the inclined physical wall for two fluids with power-law indices, $n = 0.5$ and 1 at Re $= 10$ and $\theta = 0.1$. One notable observation is that the highest error occurs in the WSS calculations, specifically at the physical wall, where the off-grid distance between the fluid node and the inclined wall is zero. However, this error can be significantly reduced by appropriately modifying the relaxation and bulk viscosity relaxation times.

A significant trend from the table is that the error rate decreases as the distance between the fluid node and the physical wall increases. This emphasizes the significance of measuring WSS distributions at locations far from the physical wall to obtain precise simulation results. By doing so, we can improve the reliability of WSS predictions, especially for fluid flows with highly non-Newtonian behavior with low values of n.

From this perspective, we present the errors in the distribution of WSS for different flows of shear-thinning power-law fluids in an inclined channel with varying inclinations and Re $= 10$, as demonstrated in Fig. 22. The error surface plots reveal that, in general, the MRT collision operator [Fig. 22(b)] yields more accurate WSS distributions than the BGK method [Fig. 22(a)].

Figure 22(c) illustrates the errors in the distribution of WSS after modifying the relaxation time of bulk viscosity using Eq. (23). Remarkably, this modification results in higher accuracy when simulating WSS distributions at all inclinations, significantly reducing error rates. Findings suggest that the MRT collision operator outperforms BGK in simulating WSS distributions. By appropriately adjusting the relaxation time for bulk viscosity, we can achieve even greater accuracy,

TABLE IV. Comparison of the calculated analytical WSS distribution with MRT and tuned MRT collision at 10 nodes near the inclined physical wall for two different fluids with power-law indices, $n = 0.5$ and 1 at Re $= 10$ and $\theta = 0.1$.

	$n = 0.5$			$n = 1.0$		
Off-grid distance	MRT	MRT with Eq (23)	Theoretical WSS	MRT	Tuned MRT with Eq. (23)	Theoretical WSS
0	0.7655×10^{-2}	0.8224×10^{-2}	0.8382×10^{-2}	0.2488×10^{-4}	0.2482×10^{-4}	0.2514×10^{-4}
0.8955	0.7342×10^{-2}	0.7923×10^{-2}	0.7897×10^{-2}	0.2400×10^{-4}	0.2391×10^{-4}	0.2369×10^{-4}
0.7960	0.7402×10^{-2}	0.7984×10^{-2}	0.7951×10^{-2}	0.2419×10^{-4}	0.2412×10^{-4}	0.2385×10^{-4}
0.6965	0.7445×10^{-2}	0.8027×10^{-2}	0.8005×10^{-2}	0.2429×10^{-4}	0.2421×10^{-4}	0.2401×10^{-4}
0.5970	0.7489×10^{-2}	0.8077×10^{-2}	0.8059×10^{-2}	0.2440×10^{-4}	0.2432×10^{-4}	0.2417×10^{-4}
0.4975	0.7530×10^{-2}	0.8112×10^{-2}	0.8113×10^{-2}	0.2451×10^{-4}	0.2443×10^{-4}	0.2433×10^{-4}
0.3980	0.7558×10^{-2}	0.8141×10^{-2}	0.8166×10^{-2}	0.2462×10^{-4}	0.2454×10^{-4}	0.2450×10^{-4}
0.2985	0.7577×10^{-2}	0.8158×10^{-2}	0.8220×10^{-2}	0.2472×10^{-4}	0.2464×10^{-4}	0.2466×10^{-4}
0.1990	0.7602×10^{-2}	0.8184×10^{-2}	0.8274×10^{-2}	0.2480×10^{-4}	0.2477×10^{-4}	0.2482×10^{-4}
0.0995	0.7637×10^{-2}	0.8206×10^{-2}	0.8328×10^{-2}	0.2485×10^{-4}	0.2476×10^{-4}	0.2498×10^{-4}

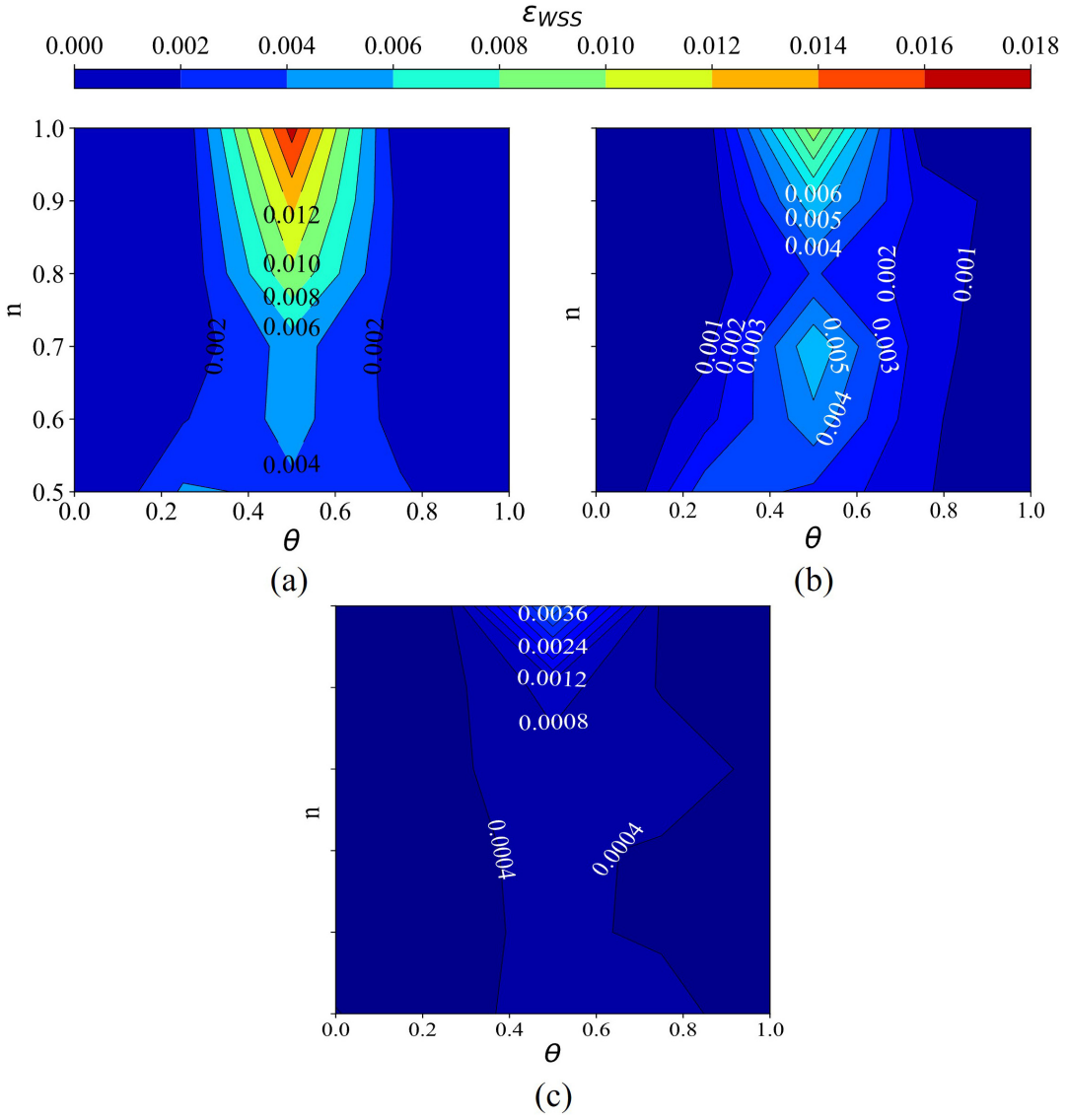

FIG. 22. Wall shear stress (WSS) distribution errors for various shear-thinning power-law fluid flows in an inclined channel with varying inclinations and Re = 10 using (a) Bhatnagar-Gross-Krook (BGK), (b) multiple relaxation time (MRT), and (c) tuned MRT collisions.

particularly in inclined channels with shear-thinning power-law fluids at Re = 10.

IV. SUMMARY AND CONCLUSIONS

In this paper, we have conducted a comprehensive analysis of the applicability of the LBM to simulate non-Newtonian fluids, particularly the accuracy of WSS. We systematically examine the use of BGK and MRT collision operators for non-Newtonian power-law fluids in the vicinity of off-grid geometries. Our focus has been to identify the numerical errors resulting from how rheological properties of non-Newtonian fluids are simulated in LBM, how different boundary conditions are implemented, the effect of interpolated curved geometries, and the choice of collision operators in the LBM context. We examined that employment of the IBB method is more crucial for conducting LBM simulations of WSS and non-Newtonian fluids, as these fluids exhibit higher sensitivity to boundary conditions owing to their complex rheological properties.

Due to a limited number of cases with known analytical solutions, we focused on the non-Newtonian power-law model in a Hagen-Poiseuille flow between two plates. We have examined channel flows under two separate conditions, one driven by a constant body force and the other by pressure differences. This strategy revealed significant difference in accuracy in how WSS was estimated in the BGK and MRT scenarios. The main reason for the difference is that the LBM displays a form of pseudocompressibility when pressure boundary conditions are implemented; these compressibility effects become very important to handle for power-law fluids.

It is important to acknowledge that various non-Newtonian models exist which can more accurately simulate shear-viscosity profiles and capture the complex behaviors of different fluids. Incorporating these models could potentially yield more realistic results. The selection of a specific non-Newtonian model influences the outcomes and accuracy of

simulations. Therefore, the findings presented in this paper could serve as a reference for adjusting simulation parameters when employing alternative non-Newtonian models, thereby enhancing the realism and precision of the simulations.

Based on our findings the MRT method for power-law fluids improves numerical accuracy in the simulation of WSS distributions, especially in off-grid geometries compared with the standard BGK collision operator. Through systematic investigation, we have identified that MRT, with adequately tuned relaxation times, not only enhances numerical stability and accuracy but also ensures better mass conservation and reduces compressibility effects inherent in the LBM method. Results conclusively demonstrate that MRT collision operators are superior to BGK in handling non-Newtonian fluids, offering a more accurate representation of WSS distributions and improving overall simulation stability. In this paper, we also reveal that non-Newtonian flows are more susceptible to mass imbalance caused by the interpolations of the physical walls and viscosity-dependent discrepancies at bounce-back walls than Newtonian assumption, which the MRT approach can effectively address. This means decoupling each moment and relaxing toward equilibrium at its own rate can accurately represent the physical processes occurring in the fluid. This is beneficial for non-Newtonian fluids, where the relationship between stress and strain rate is nonlinear and can vary spatially within the flow. Applying MRT collision operator is particularly crucial in pressure-driven flows where bulk viscosity plays a significant role, an aspect often neglected in Newtonian simulations but critical for accurately adapting to rapid changes in local effective viscosity in non-Newtonian fluids. Hence, the findings underscore the necessity of reevaluating the suitability of BGK operators for non-Newtonian simulations and advocate for broader adoption of MRT operators to enhance the fidelity of LBM simulations involving non-Newtonian fluids and off-grid boundaries.

The data that support the findings in this paper are available from the corresponding author upon reasonable request.

ACKNOWLEDGMENT

The authors would like to thank the financial support provided by the Equinor Academia Program.

[1] P. F. Davies, Flow-mediated endothelial mechanotransduction, Physiol Rev. **75**, 519 (1995).

[2] D. G. Katritsis, Upper and lower common pathways in atrioventricular nodal reentrant tachycardia: Refutation of a legend? Pacing. Clin. Electrophysiol. **30**, 1305 (2007).

[3] R. P. Chhabra and J. F. Richardson, *Non-Newtonian Flow in the Process Industries: Fundamentals and Engineering Applications* (Butterworth-Heinemann, Oxford, 1999).

[4] J. R. A. Pearson and P. M. J. Tardy, Models for flow of non-Newtonian and complex fluids through porous media, J. Non-Newtonian Fluid Mech. **102**, 447 (2002).

[5] B. C. Bell and K. S. Surana, *p*-version least squares finite element formulation for two-dimensional, incompressible, non-Newtonian isothermal and non-isothermal fluid flow, Int. J. Numer. Methods Fluids **18**, 127 (1994).

[6] T. C. Papanastasiou and A. G. Boudouvis, Flows of viscoplastic materials: Models and computations, Comput. Struct. **64**, 677 (1997).

[7] P. Neofytou, A 3rd order upwind finite volume method for generalised Newtonian fluid flows, Adv. Eng. Software **36**, 664 (2005).

[8] S. Chen, D. Martínez, and R. Mei, On boundary conditions in lattice Boltzmann methods, Phys. Fluids **8**, 2527 (1996).

[9] T.-H. Wu and D. Qi, Lattice-Boltzmann lattice-spring simulations of influence of deformable blockages on blood fluids in an elastic vessel, Comput. Fluids **155**, 103 (2017).

[10] J. Boyd, J. Buick, and S. Green, A second-order accurate lattice Boltzmann non-Newtonian flow model, J. Phys. A: Math. Gen. **39**, 14241 (2006).

[11] M. Yoshino, Y. Hotta, T. Hirozane, and M. Endo, A numerical method for incompressible non-Newtonian fluid flows based on the lattice Boltzmann method, J. Non-Newtonian Fluid Mech. **147**, 69 (2007).

[12] H. Wei, C. S. Herrington, J. D. Cleveland, V. A. Starnes, and N. M. Pahlevan, Hemodynamically efficient artificial right atrium design for univentricular heart patients, Phys. Rev. Fluids **6**, 123103 (2021).

[13] S. A. Hosseini, F. Huang, and D. Thévenin, Lattice Boltzmann model for simulation of flow in intracranial aneurysms considering non-Newtonian effects, Phys. Fluids **34**, 073105 (2022).

[14] V. Dzanic, C. S. From, and E. Sauret, Assessment of polymer feedback coupling approaches in simulation of viscoelastic fluids using the lattice Boltzmann method, Comput. Fluids **246**, 105629 (2022).

[15] M. Bisht and D. V. Patil, Power-law fluid flow in driven enclosures with undulation using MRT-lattice Boltzmann method, Comput. Math. Appl. **79**, 100 (2020).

[16] M. Bisht and D. V. Patil, Assessment of multiple relaxation time-lattice Boltzmann method framework for non-Newtonian fluid flow simulations, Eur. J. Mech. B/Fluids **85**, 322 (2021).

[17] L. Jahanshaloo, N. A. C. Sidik, A. Fazeli, and M. P. H. A., An overview of boundary implementation in lattice Boltzmann method for computational heat and mass transfer, Int. Commun. Heat Mass Transf. **78**, 1 (2016).

[18] M. Bouzidi, M. Firdaouss, and P. Lallemand, Momentum transfer of a Boltzmann-lattice fluid with boundaries, Phys. Fluids **13**, 3452 (2001).

[19] Z. Wang, Y. Wei, and Y. Qian, A bounce back-immersed boundary-lattice Boltzmann model for curved boundary, Appl. Math. Model. **81**, 428 (2020).

[20] C.-H. Lee, Z. Huang, and Y.-M. Chiew, An extrapolation-based boundary treatment for using the lattice Boltzmann method to simulate fluid-particle interaction near a wall, Eng. Appl. Comput. Fluid Mech. **9**, 370 (2015).

[21] A. J. C. Ladd, Numerical simulations of particulate suspensions via a discretized Boltzmann equation. Part 1. Theoretical foundation, J. Fluid Mech. **271**, 285 (2006).

[22] Z.-Q. Dong, L.-P. Wang, C. Peng, and T. Chen, A systematic study of hidden errors in the bounce-back scheme and their

various effects in the lattice Boltzmann simulation of viscous flows, Phys. Fluids **34**, 2 (2022).
[23] D. d'Humières, Multiple-relaxation-time lattice Boltzmann models in three dimensions, Phil. Trans. R. Soc. A **360**, 437 (2002).
[24] J. C. Verschaeve, Analysis of the lattice Boltzmann Bhatnagar-Gross-Krook no-slip boundary condition: Ways to improve accuracy and stability, Phys. Rev. E **80**, 036703 (2009).
[25] B. Stahl, B. Chopard, and J. Latt, Measurements of wall shear stress with the lattice Boltzmann method and staircase approximation of boundaries, Comput. Fluids **39**, 1625 (2010).
[26] I. Ginzburg, and D. d'Humières, Multireflection boundary conditions for lattice Boltzmann models, Phys. Rev. E. **68**, 066614 (2003).
[27] I. Ginzbourg and P. M. Adler, Boundary flow condition analysis for the three-dimensional lattice Boltzmann model, J. Phys. II France **4**, 191 (1994).
[28] X. He, Q. Zou, L.-S. Luo, and M. Dembo, Analytic solutions of simple flows and analysis of nonslip boundary conditions for the lattice Boltzmann BGK model, J. Stat. Phys. **87**, 115 (1997).
[29] X. Kang and Z. Dun, Accuracy and grid convergence of Wall shear stress measured by lattice Boltzmann method, Int. J. Mod. Phys. C **25**, 1450057 (2014).
[30] Y. Shimogonya, T. Ishikawa, Y. Imai, N. Matsuki, and T. Yamaguchi, Can temporal fluctuation in spatial wall shear stress gradient initiate a cerebral aneurysm? A proposed novel hemodynamic index, the gradient oscillatory number (GON), J. Biomech. **42**. 550 (2009).
[31] X. Kang, Assessment of the pulsatile wall shear stress in the stenosed and recanalized carotid bifurcations by the lattice Boltzmann method, Comput. Fluids **97**, 156 (2014).
[32] H. Karimpour and E. Javdan, Simulation of stenosis growth in the carotid artery by lattice Boltzmann method, J. Mech. Med. Biol. **14**, 1450016 (2014).
[33] H. H. Afrouzi, M. Ahmadian, M. Hosseini, H. Arasteh, D. Toghraie, and S. Rostami, Simulation of blood flow in arteries with aneurysm: Lattice Boltzmann approach (LBM), Comput. Methods Prog Biomed **187**, 105312 (2020).
[34] Z.-G. Feng and E. E. Michaelides, The immersed boundary-lattice Boltzmann method for solving fluid-particles interaction problems, J. Comput. Phys. **195**, 602 (2004).
[35] O. R. Mohammadipoor, H. Niazmand, and S. A. Mirbozorgi, Alternative curved-boundary treatment for the lattice Boltzmann method and its application in simulation of flow and potential fields, Phys. Rev. E **89**, 013309 (2014).
[36] A. Tiwari and S. P. Vanka, A ghost fluid lattice Boltzmann method for complex geometries, Int. J. Numer. Methods Fluids **69**, 481 (2011).
[37] J. Boyd, J. M. Buick, and S. Green, Analysis of the Casson and Carreau-Yasuda non-Newtonian blood models in steady and oscillatory flows using the lattice Boltzmann method, Phys. Fluids **19**, 093103 (2007).
[38] K. Khellaf and G. Lauriat, Numerical study of heat transfer in a non-Newtonian Carreau-fluid between rotating concentric vertical cylinders, J. Non-Newtonian Fluid Mech. **89**, 45 (2000).
[39] H. Zhu, Y. D. Kim, and D. De Kee, Non-Newtonian fluids with a yield stress, J. Non-Newtonian Fluid Mech. **129**, 177 (2005).
[40] Y. Li, R. Shock, R. Zhang, and H. Chen, Numerical study of flow past an impulsively started cylinder by the lattice-Boltzmann method, J. Fluid Mech. **519**, 273 (2004).
[41] P. Nathen, D. Gaudlitz, M. J. Krause, and N. A. Adams, On the stability and accuracy of the BGK, MRT and RLB Boltzmann schemes for the simulation of turbulent flows, Commun. Comput Phys. **23**, 846 (2018).
[42] E. Jettestuen, O. Aursjø, J. L. Vinningland, and A. Hiorth, A generalized bodyforce scheme for lattice Boltzmann simulations of incompressible flow in complex geometries, Phys. Fluids **35**, 027122 (2023).
[43] E. Ezzatneshan and H. Vaseghnia, Simulation of collapsing cavitation bubbles in various liquids by lattice Boltzmann model coupled with the Redlich-Kwong-Soave equation of state, Phys. Rev. E **102**, 053309 (2020).
[44] P. Lallemand and L. S. Luo, Theory of the lattice boltzmann method: Dispersion, dissipation, isotropy, Galilean invariance and stability, Phys. Rev. E **61**, 6546 (2000).
[45] Z. Guo, C. Zheng, and B. Shi, Discrete lattice effects on the forcing term in the lattice Boltzmann method, Phys. Rev. E **65**, 046308 (2002).
[46] E. Ezzatneshan, A. Salehi, and H. Vaseghnia, Study on forcing schemes in the thermal lattice Boltzmann method for simulation of natural convection flow problems, Heat Transfer **50**. 7604 (2021).
[47] Q. Zou and X. He, On pressure and velocity boundary conditions for the lattice Boltzmann BGK model, Phys. Fluids **9**, 1591 (1997).
[48] T. Krüger, H. Kusumaatmaja, A. Kuzmin, O. Shardt, G. Silva, and E. M. Viggen, *The Lattice Boltzmann Method: Principles and Practice* (Springer International Publishing, Cham, 2017).